AD_____

Award Number: W81XWH-07-1-0058

TITLE: Cone-Beam Computed Tomography for Image-Guided Radiation Therapy of Prostate Cancer

PRINCIPAL INVESTIGATOR: Seungryong Cho

CONTRACTING ORGANIZATION: University of Chicago
Chicago, IL 60637

REPORT DATE: January 2009

TYPE OF REPORT: Annual Summary

PREPARED FOR: U.S. Army Medical Research and Materiel Command
Fort Detrick, Maryland 21702-5012

REPORT DOCUMENTATION PAGE

Form Approved
OMB No. 0704-0188

1. REPORT DATE *(DD-MM-YYYY)*	**2. REPORT TYPE**	**3. DATES COVERED** *(From - To)*
01-01-2008	Annual Summary	11 DEC 2007 - 11 DEC 2008

4. TITLE AND SUBTITLE

Cone-Beam Computed Tomography for Image-Guided Radiation Therapy of Prostate Cancer

5a. CONTRACT NUMBER

5b. GRANT NUMBER
W81XWH-07-1-0058

5c. PROGRAM ELEMENT NUMBER

6. AUTHOR(S)
Seungryong Cho

E-Mail: srcho@uchicago.edu

5d. PROJECT NUMBER

5e. TASK NUMBER

5f. WORK UNIT NUMBER

7. PERFORMING ORGANIZATION NAME(S) AND ADDRESS(ES)

University of Chicago
Chicago, IL 60637

8. PERFORMING ORGANIZATION REPORT NUMBER

9. SPONSORING / MONITORING AGENCY NAME(S) AND ADDRESS(ES)
U.S. Army Medical Research and Materiel Command
Fort Detrick, Maryland 21702-5012

10. SPONSOR/MONITOR'S ACRONYM(S)

11. SPONSOR/MONITOR'S REPORT NUMBER(S)

12. DISTRIBUTION / AVAILABILITY STATEMENT
Approved for Public Release; Distribution Unlimited

13. SUPPLEMENTARY NOTES

14. ABSTRACT The success of intensity-modulated radiation therapy (IMRT) or 4-D conformal radiation therapy (CRT) is heavily reliant on accurate image-guidance in prostate cancer treatment. Cone-beam computed tomography (CBCT) is becoming one of the dominant imaging modalities for image-guidance, but current technology based on Feldkamp algorithm for image reconstruction from a circular scanning trajectory does not yield sufficient quality of images. In addition, imaging-radiation dose is one of the key issues, which has to be minimized or optimized. We report our continued research on CBCT scanning methods and corresponding image reconstruction algorithms that can increase the accuracy of the images and/or reduce patient dose from CBCT. A BPF-FBP tandem algorithm for reverse helical CBCT has been developed, intensity-weighted region-of-interest image reconstruction methods have been explored, and a prior-image-based few-view CBCT approach has been proposed.

15. SUBJECT TERMS
Cone-beam computed tomography, image-guided radiation therapy, region-of-interest, few-view

16. SECURITY CLASSIFICATION OF:			**17. LIMITATION OF ABSTRACT**	**18. NUMBER OF PAGES**	**19a. NAME OF RESPONSIBLE PERSON**
a. REPORT	**b. ABSTRACT**	**c. THIS PAGE**			USAMRMC
U	U	U	UU	53	**19b. TELEPHONE NUMBER** *(include area code)*

Table of Contents

Page

INTRODUCTION

The success of intensity-modulated radiation therapy (IMRT) or 4-D conformal radiation therapy (CRT) is reliant heavily on accurate image-guidance in prostate cancer treatment. Cone-beam CT (CBCT) image acquisition is becoming one of the dominant imaging modalities, and the accuracy of CBCT images and the radiation dose of CBCT imaging are considered important issues [1,2]. Most scanning geometries of CBCT used in prostate cancer treatment are circular trajectories, which yield insufficient data for theoretically exact volumetric image reconstruction. As a consequence, images reconstructed by approximate algorithms, mostly based on the Feldkamp algorithm, often contain artifacts such as streaks, intensity drop, and image deformation in regions away from the trajectory plane [3]. Radiation dose to the prostate cancer patient due to CBCT should be carefully studied, and imaging schemes that can lead to minimum dose should be devised, if interplay between imaging and therapeutic dose conformity is considered, This is of high importance especially in repeated scans during the treatment process for potentially adapting treatment plans to changes in prostate over time. The overall objective of this project is to investigate and develop innovative CBCT scanning methods and corresponding reconstruction algorithms for enhancing image accuracy of the patient's prostate and/or for reducing patient dose in CBCT. During the second year of the traineeship, image reconstruction algorithm of a short object in the reverse helical CBCT has been developed, an algorithm is under investigation for a long object image reconstruction, intensity-weighted region-of-interest (IWROI) reconstruction methods have been developed to reduce imaging radiation dose, and an updated few-view CBCT approach has also been proposed for reduction of imaging radiation dose. This report summarizes the progress of this Predoctoral Traineeship Award project made by the recipient during the past one year.

BODY

1 Training Accomplishments

At the time of this report, the recipient, Seungryong Cho, of the Predoctoral Traineeship Award has taken 22 out of 22 required courses towards his Ph.D. degree in medical physics. The courses include physics of medical imaging, physics of radiation therapy, mathematics for medical physicists, image guided radiation therapy, statistics, anatomy of the body, radiation biology and teaching assistantship.

2 Research Accomplishments

2.1 Investigation of reconstruction algorithms for reverse helical CBCT

Helical scanning configuration is used widely in diagnostic CBCT for acquiring data sufficient for exact image reconstruction over an extended volume. In image-guided radiation therapy (IGRT) and other applications of CBCT, it is difficult, if not impossible, to implement mechanically a multiple-turn helical trajectory on the imaging systems due to hardware constraints. However, imaging systems in these applications often allow for the implementation of reverse helical trajectories in which the rotation direction changes between two turns. Image reconstruction algorithms have been investigated for this novel scanning configuration. The recently developed chord-based backprojection-filtration (BPF) algorithm has been applied to the reverse helical CBCT, and it was shown that chordless regions exist in which no images can thus be reconstructed by use of the chord-based algorithms. A shift-invariant filtered backprojection (FBP) algorithm that does not depend upon the chords has therefore been developed for volumetric image reconstruction in a reverse helical CBCT [4].

However, the proposed FBP algorithm cannot handle a long object that extends beyond the reverse helix along the longitudinal direction. Therefore, a hybrid approach has been investigated for solving the long object problem in the reverse helical CBCT, and a BPF-FBP tandem algorithm has been developed [5]. In this approach, a chord-based BPF algorithm is first applied and the reconstructed volume image is reprojected and subtracted from the original cone-beam data so that the FBP algorithm can reconstruct the chordless region of the volume image. The manuscript on this hybrid approach is currently in preparation and the previous work published in *Medical Physics* is attached as Appendix A.

2.2 Investigation of IWROI image reconstruction in circular CBCT

As an attempt to reduce patient dose, scanning time, and scatter to the detector, we have investigated algorithms for ROI image reconstruction in CBCT. A backprojection-filtration (BPF) algorithm based on chords has been developed to reconstruct ROI images from truncated data set which contains only the projections of the ROI in a circular scan. It was observed, however, that the ROI reconstructible by the chord-based algorithms cannot be exclusively the treatment target in general. The ROI usually contains more than the target including those organs sensitive to the radiation. In this regard, we proposed an innovative, intensity-weighted ROI imaging technique to lower patient dose to the normal tissue surrounding the target and at the same time to preserve the image quality of the target in

the ROI. The ROI in this task is divided into two subROI's. Higher dose is delivered to the inner ROI containing the target, and lower dose is to the outer ROI. Each projection image, therefore, will have different noise levels in two regions: inner ROI projection and outer ROI projection.

Clinical feasibility of the IWROI imaging was investigated with the on-board imaging (OBI) system on a Trilogy linear accelerator (Varian Medical Systems) [6]. The OBI system is composed of an x-ray source and flat panel detector mounted on the accelerator gantry orthogonal to the treatment beam. A nonuniform filter is placed in the x-ray beam to create regions of two different beam intensities. In this manner, regions outside the target area can be given a reduced dose but still visualized with a lower contrast-to-noise-ratio (CNR). Image artifacts due to transverse data truncation, which would have occurred in conventional reconstruction algorithms, are avoided and image noise levels of the low and high-intensity regions are well controlled by use of the chord-based BPF reconstruction algorithm. A preliminary measurement of dose reduction has been performed [7], and we believe the proposed IWROI technique can play an important role in prostate IGRT. The details of the work are attached as Appendix B.

2.3 Investigation of few-view CBCT for IGRT

As another attempt to reduce patient dose, scanning time, we have investigated a few-view CBCT for IGRT. One unique feature of CBCT for interfraction motion detection is the availability of prior anatomical images, which contains no substantial changes. A prior image may be available from the previous fraction CBCT scan, or an initial CBCT set-up scan. These scans contain the same anatomical information as the current scan except for anatomical changes due to internal motion or patient weight gain/loss. However, a substantial portion of the image, particularly including bony structures and surrounding tissues, remains unchanged. We proposed an iterative algorithm for image reconstruction from a very limited number of projections in CBCT, which is based on minimization of the image total-variation (TV) subject to the constraints of data fidelity and positivity and that utilizes information available from a prior image [8].

We have previously proposed a TV algorithm utilizing prior image with internal motion as an initial guess in few-view fan-beam CT, and successfully demonstrated that the number of views for image reconstruction can be reduced from that needed in the TV algorithm without prior in the numerical study (roughly speaking, from 20 views to 10 views) [9]. Using the prior image as an initial image estimate in the iterative process is thought to help find the true minimum TV image that meets the data fidelity constraint, whereas a local minimum may be found when no prior image information is used. However, it was observed that the unchanged portion of the prior image, which is controlled in the numerical study, could be vulnerable to changes as the iteration steps advance and may degrade when the amount of projection data is extremely limited (e.g. five views). In the modified work, we mask the image region that is unchanged from the prior image so that the masked region is not influenced by the updates during iterative steps. We showed in numerical simulations that successful image reconstruction can be realized from five views. The preliminary study has been accepted for an oral presentation at *the SPIE Medical Imaging Conference, 2009.* The paper is also attached as Appendix C.

KEY RESEARCH ACCOMPLISHMENTS

- We have previously proposed a novel image acquisition geometry of reverse helix for CBCT imagers mounted on LINAC treatment systems used for prostate cancer IGRT, and developed an exact image reconstruction algorithm for a short object within the reverse helix.
- We have proposed a hybrid approach and developed a BPF-FBP tandem algorithm for image reconstruction of a long object in the reverse helical CBCT.
- We have investigated the clinical feasibility of an IWROI imaging for prostate cancer IGRT using the OBI system on a Trilogy linear accelerator (Varian Medical Systems).
- We have conducted a preliminary measurement of dose reduction via IWROI imaging and reported a reduction of 37 %. The proposed method can therefore bring in useful outcomes in terms of dose management and image-guidance.
- We have performed a preliminary, but substantial, numerical study of a prior-image-based few-view CBCT for prostate cancer IGRT based on TV algorithms. Successful implementation of the proposed imaging technique to the clinical setting can lead to a significant reduction of imaging dose.

REPORTABLE OUTCOMES

Peer-reviewed Journal Articles

1. **S. Cho**, D. Xia, C. A. Pelizzari, and X. Pan: Exact reconstruction of volumetric images in reverse helical cone-beam CT, Med. Phys., **35**, pp. 3030-3040, 2008.

2. **S. Cho**, E. Pearson, C. A. Pelizzari, and X. Pan: Region-of-interest imaging with intensity-weighting in circular cone-beam CT for image-guided radiation therapy, Med. Phys. (accepted with revision), 2008.

3. D. Xia, **S. Cho**, and X. Pan: Image reconstruction for a reduced scan in circular sinusoidal cone-beam CT, Opt. Engr., (submitted), 2008.

4. **S. Cho**, C. A. Pelizzari, and X. Pan: A BPF-FBP tandem algorithm for image reconstruction in reverse helical cone-beam computed tomography, (in preparation), 2009

Conference Proceeding Articles

1. D. Xia, **S. Cho**, J. Bian, E. Sidky, C. A. Pelizzari, and X. Pan: Tomosynthesis with source distributions over a surface, Proc. SPIE, Vol. 6913, 69132A, 2008.

2. **S. Cho**, E. Sidky, C. A. Pelizzari, and X. Pan: A preliminary investigation of using prior information for potentially improving image reconstruction in few-view CT, Proc. SPIE, Vol. 6913, 69132C, 2008.

3. **S. Cho**, E. Pearson, D. Xia, X. Han, C. A. Pelizzari, and X. Pan: A preliminary study of intensity-weighted ROI imaging in cone-beam CT, Proc. SPIE, Vol. 6913, 691325, 2008.

Conference Presentations and Abstracts

1. **S. Cho**, E. Pearson, C. A. Pelizzari, and X. Pan: Image artifacts caused by the extra focal spot of an x-ray tube in cone-beam computed tomography, AAPM, Houston, TX, 2008.

2. E. Pearson, **S. Cho**, X. Pan, and C. A. Pelizzari: Dose reduction in CBCT via intensity-weighted region-of-interest imaging, AAPM, Houston, TX, 2008.

3. E. Pearson, **S. Cho**, X. Pan, and C. A. Pelizzari: Region-of-interest imaging for cone-beam CT in radiation therapy, Varian Research Partnership Symposium, Austin, TX, 2008.

4. D. Xia, **S. Cho**, and X. Pan: Backprojection-filtration reconstruction without invoking a spatially varying weighting factor, IEEE MIC, Dresden, Germany, 2008.

5. **S. Cho**, E. Pearson, E. Sidky, J. Bian, C. A. Pelizzari, and X. Pan: Prior-image-based few-view cone-beam CT for applications to daily scan in image-guided radiation therapy: Preliminary study, accepted for oral presentation in SPIE Medical Imaging Conference, 2009.

6. **S. Cho**, E. Pearson, C. A. Pelizzari, and X. Pan: Noise analysis in intensity-weighted region-of-interest imaging for cone-beam CT, accepted for oral presentation in SPIE Medical Imaging Conference, 2009.

Honors and Awards

- The Carl J. Vyborny Journal Club Award, Graduate Programs in Medical Physics, The University of Chicago, 2008
- Paul C. Hodges Research Award, Department of Radiology, The University of Chicago, 2008

CONCLUSIONS

The recipient of the Predoctoral Traineeship Award has finished the required courses towards his Ph.D. degree. These trainings have proven useful for the recipient to achieve the proposed research goals.

During the second year, we have continued to investigate innovative approaches in cone-beam CT for IGRT that can increase the accuracy of the reconstructed images and/or reduce radiation dose to the patient having prostate cancer. A BPF-FBP tandem image reconstruction algorithm has been proposed for prostate IGRT using a reverse helical CBCT scan. An IWROI imaging method has been proposed for sparing imaging radiation dose to the surrounding tissues and overall dose to the patient as well, and its clinical feasibility has been successfully investigated. A prior-image-based few-view CBCT technique has been proposed, and the preliminary results of a numerical study suggest its potential usefulness in prostate IGRT.

Overall, we have achieved the goals for the second year and are well prepared for the research in the next year. Our goals in the next year include a thorough evaluation of dose reduction via IWROI imaging, an experimental demonstration of the feasibility of the prior-image-based few-view CBCT, and experimental implementation of the reverse helical CBCT; all of these will be studied in the context of applications to prostate cancer IGRT.

REFERENCES

1. D. Verellen, M. D. Ridder, N. Linthout, K. Tournel, G. Soete, and G. Storme: Innovations in image-guided radiotherapy, Nature Reviews Cancer, **7**, pp. 949-960, 2007.

2. M. J. Murphy, J. Balter, S. Balter, J. A. BenComo, I. J. Das, S. B. Jiang, C. -M. Ma, G. H. Olivera, R. F. Rodebaugh, K. J. Ruchala, H. Shirato, and F. -F. Yin: The management of imaging dose during image-guided radiotherapy: Report of the AAPM Task Group 75 , Med. Phys., **34**, pp. 4041-4063, 2007.

3. Y. Zou, A. A. Zamyatin, B. S. Chiang, and M. D. Silver: Reduction of streak artifacts in circular cone beam CT using scanograms, Proc. MIC, M18-294, 2007

4. S. Cho, D. Xia, C. A. Pelizzari, and X. Pan: Exact reconstruction of volumetric images in reverse helical cone-beam CT, Med. Phys., **35**, pp. 3030-3040, 2008.

5. S. Cho, C. A. Pelizzari, and X. Pan: A BPF-FBP tandem algorithm for image reconstruction in reverse helical cone-beam computed tomography, (in preparation), 2009

6. S. Cho, E. Pearson, C. A. Pelizzari, and X. Pan: Region-of-interest imaging with intensity-weighting in circular cone-beam CT for image-guided radiation therapy, Med. Phys. (accepted with revision), 2008.

7. E. Pearson, S. Cho, X. Pan, and C. A. Pelizzari: Dose reduction in CBCT via intensity-weighted region-of-interest imaging, Med. Phys. **35**, pp. 2641, 2008.

8. S. Cho, E. Pearson, E. Sidky, J. Bian, C. A. Pelizzari, X. Pan: Prior-image-based few-view cone-beam CT for applications to daily scan in image-guided radiation therapy: Preliminary study, Proc. SPIE Medical Imaging Conference (to be published), 2009.

9. S. Cho, E. Y. Sidky, C. A. Pelizzari, and X. Pan: Few-view cone-beam computed tomography for image-guided radiation therapy , Proc. SPIE, Vol. 6913, 69132C, 2008.

APPENDICES

- Appendix A: S. Cho, D. Xia, C. A. Pelizzari, and X. Pan: Exact reconstruction of volumetric images in reverse helical cone-beam CT, Med. Phys., 35, pp. 3030-3040, 2008.
- Appendix B: S. Cho, E. Pearson, C. A. Pelizzari, and X. Pan: Region-of-interest imaging with intensity-weighting in circular cone-beam CT for image-guided radiation therapy, Med. Phys. (accepted with revision), 2008.
- Appendix C: S. Cho, E. Pearson, E. Sidky, J. Bian, C. A. Pelizzari, X. Pan: Prior-image-based few-view cone-beam CT for applications to daily scan in image-guided radiation therapy: Preliminary study, (to be published) Proc. SPIE Medical Imaging Conference, 2009.

Exact reconstruction of volumetric images in reverse helical cone-beam CT

Seungryong Cho
Department of Radiology and Department of Radiation and Cellular Oncology, University of Chicago, Illinois 60637

Dan Xia
Department of Radiology, University of Chicago, Chicago, Illinois 60637

Charles A. Pelizzari
Department of Radiation and Cellular Oncology, University of Chicago, Chicago, Illinois 60637

Xiaochuan Pan[a)]
Department of Radiology, University of Chicago, Chicago, Illinois 60637

(Received 26 December 2007; revised 22 April 2008; accepted for publication 23 April 2008; published 12 June 2008)

Helical scanning configuration has been used widely in diagnostic cone-beam computed tomography (CBCT) for acquiring data sufficient for exact image reconstruction over an extended volume. In image-guided radiation therapy (IGRT) and other applications of CBCT, it can be difficult, if not impossible, to implement mechanically a multiple-turn helical trajectory on the imaging systems due to hardware constraints. However, imaging systems in these applications often allow for the implementation of a reverse helical trajectory in which the rotation direction changes between two consecutive turns. Because the reverse helical trajectory satisfies Tuy's condition, when projections of the imaged object are nontruncated, it yields data sufficient for exact image reconstruction within the reverse helix volume. The recently developed chord-based algorithms such as the backprojection filtration (BPF) algorithm can readily be applied to reconstructing images on chords of a reverse helical trajectory, and they can thus reconstruct an image within a volume covered by the chords. Conversely, the chord-based algorithms cannot reconstruct images within regions that are not intersected by chords. In a reverse helix volume, as shown below, chordless regions exist in which no images can thus be reconstructed by use of the chord-based algorithms. In this work, based upon Pack–Noo's formula, a shift-invariant filtered backprojection (FBP) algorithm is derived for exact image reconstruction within the reverse helix volume, including the chordless region. Numerical studies have also been conducted to demonstrate the chordless region in a reverse helix volume and to validate the FBP algorithm for image reconstruction within the chordless region. Results of the numerical studies confirm that the FBP algorithm can exactly reconstruct an image within the entire reverse helix volume, including the chordless region. It is relatively straightforward to extend the FBP algorithm to reconstruct images for general trajectories, including reverse helical trajectories with variable pitch, tilted axis, and/or additional segments between turns. [DOI: 10.1118/1.2936219]

Key words: cone-beam computed tomography, reconstruction, reverse helical, filtered backprojection, image-guided radiation therapy

I. INTRODUCTION

Computed tomography (CT) is used widely as one of the leading imaging modalities in image-guided radiation therapy (IGRT). In the last few years, cone-beam CT (CBCT) with a KV source that is mounted on the rotation gantry of a linear accelerator (LINAC) treatment system has become commercially available.[1–3] Integration of such a KV-CT imaging component into the LINAC system allows the KV-imaging and MV-treatment processes to share identical spatial, and temporal information about the treated patient. Currently, a KV-CT imaging scanner mounted on LINAC treatment system acquires cone-beam data by use of a scanning configuration in which the x-ray source and the detector move along a circular trajectory, largely because the mechanical implementation of a circular configuration is relatively easy. The FDK algorithm[4] and its variations have been proposed, and widely used in practice, for reconstructing approximate images from circular cone-beam data. However, due to data insufficiency, there may exist cone-beam image artifacts that include intensity drop, streak artifacts, and image deformation in reconstructed images.[5,6] The image artifacts would become more serious when a larger cone angle is used for acquiring data.

The helical source trajectory has become a standard scanning configuration in diagnostic CT because it can collect cone-beam data sufficient for exact reconstruction of volume images. Diagnostic CT achieves an extended longitudinal coverage by use of the slip-ring technology, which allows the x-ray source and the detector to rotate multiple turns continuously in one direction, while the patient couch is translated at a constant speed along one direction, thus forming a

multiple-turn helical source trajectory. The LINAC-mounted KV cone-beam CT, however, can rotate only one turn in either direction, and must reverse rotation direction after each turn. Therefore, the LINAC-mounted KV cone-beam CT imager can achieve only a one-turn helical source trajectory without altering the couch motion mode. It is expected that certain image-guided radiation therapy (IGRT) applications based on cone-beam CT images may benefit from an extended volume coverage of the patient.[7] Although single-turn helical trajectory offers some extension of the imaged volume, it may be desirable to achieve an extended longitudinal coverage beyond that of a one-turn helical trajectory. One natural way to extend the longitudinal coverage is that the couch is translated continuously along one direction while the LINAC gantry reverses its rotation direction after each turn, thus resulting in a multiple-turn reverse helical trajectory.

In this work, we investigate image reconstruction from cone-beam data acquired with reverse helical trajectories. In the last several years, significant advances have been made in algorithm development for accurate image reconstruction in helical CBCT, including Katsevich's filtered-backprojection-type algorithm and the chord-based algorithms.[8–10] These algorithms have also been extended to the algorithms for general source trajectories.[11–15] We first apply, in this work, the recently developed chord-based algorithm[10,13] to reconstructing images because they are directly applicable to general continuous trajectories including reverse helical trajectories. A chord is defined as a line segment connecting any two points on a continuous source trajectory; and chord-based algorithms reconstruct volume images through reconstructing images on all of the chords that intersect the volume. Because any selected volume enclosed by a conventional helical trajectory used in diagnostic CT is covered completely by chords,[16] chord-based algorithms can reconstruct images within the selected volume for a conventional helical trajectory.

As will be shown below, however, some portions of the reverse helix volume are not intersected by any chords, thus forming chordless regions in which images cannot be reconstructed by use of the chord-based algorithms. Therefore, the focus of the work is at developing a shift-invariant filtered backprojection (FBP) reconstruction algorithm for exactly reconstructing images within the entire reverse helix volume based upon Pack–Noo's formula.[17,18] We have conducted a study to analyze and demonstrate numerically the chordless region in a reverse helix volume that cannot be reconstructed by use of the chord-based algorithm. Additional numerical studies were conducted to validate the proposed FBP algorithm for image reconstruction within the chordless region. Results of the numerical studies confirm that, unlike the chord-based backprojection filtration (BPF) algorithm that can yield only an incomplete volume image, the proposed FBP algorithm can exactly reconstruct an image within the reverse helix volume. It is worthwhile to note, however, that the proposed FBP algorithm cannot be used directly for long object scan, because the algorithm involves data filtering along the longitudinal direction, along which the projection data may contain data truncation. However, it may be possible to address the long object problem by combining the chord-based BPF and the proposed FBP algorithms. It is relatively straightforward to extend the proposed FBP algorithm to reconstruct images for general trajectories, including reverse helical trajectories with variable pitch, tilted axis, and/or additional line segments between turns.

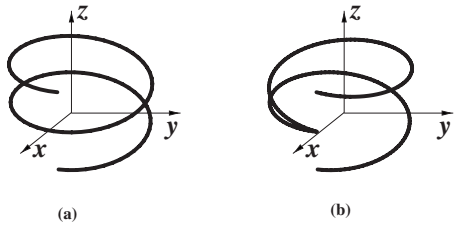

FIG. 1. A two-turn conventional helical trajectory (a) and a two-turn reverse helical trajectory (b) in the coordinate system $\{x,y,z\}$ that is fixed on the imaged object.

II. A REVERSE HELICAL TRAJECTORY

The conventional helical and reverse helical trajectories can be specified by the rotation angle λ of the source. For comparison, we give below the mathematical expressions for the two trajectories in the coordinate system that is fixed on the imaged object. For a conventional helical trajectory $\vec{r}_0(\lambda)$, it can be expressed as

$$\vec{r}_0(\lambda)=\left(R\cos\lambda,R\sin\lambda,\frac{h}{2\pi}\right),\quad \lambda\in[\lambda_s,\lambda_e], \tag{1}$$

where R denotes the distance from the source to the rotation axis, h the helical pitch, and λ_s and λ_e the starting and ending angle of the helical trajectory. In Fig. 1(a), we display a two-turn conventional helical trajectory specified by $\lambda\in[\lambda_s,\lambda_e]=[-2\pi,2\pi]$. In contrast, the reverse helical trajectory $\vec{r}_0(\lambda)$ can be written as

$$\vec{r}_0(\lambda)=\left(R\cos((-1)^n\lambda),R\sin((-1)^n\lambda),\frac{h}{2\pi}\lambda\right),$$

$$\lambda\in[\lambda_s,\lambda_e], \tag{2}$$

where integer n indicates the nth turn, and it can be written in terms of a floor function "⌊⌋" as

$$n=\left\lfloor\frac{\lambda}{2\pi}\right\rfloor+1. \tag{3}$$

Without loss of generality, we have assumed that the turn with $n=0$ in the reverse helical trajectory is a turn in the conventional helical trajectory. For example, as shown in Fig. 1, for a two-turn reverse helical trajectory specified by $\lambda\in[\lambda_s,\lambda_e]=[-2\pi,2\pi]$, we have

$$\vec{r}_0(\lambda)=\left(R\cos\lambda,R\sin\lambda,\frac{h}{2\pi}\lambda\right),\quad \lambda\in[-2\pi,0)$$

$$\vec{r}_0(\lambda)=\left(R\cos(-\lambda),R\sin(-\lambda),\frac{h}{2\pi}\lambda\right),\quad \lambda\in[0,2\pi]. \tag{4}$$

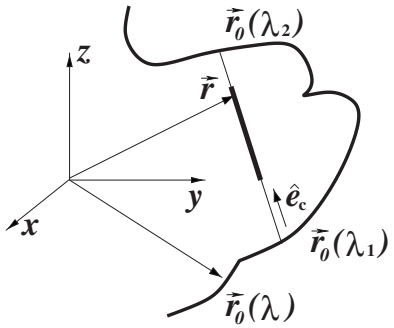

FIG. 2. Illustration of a chord (thin line segment) specified by λ_1 and λ_2 for a general, continuous trajectory. The direction of the chord is $\hat{e}_c$. The thick line segment on the chord indicates the support of the object.

Let $f(\vec{r})$ be an object function with a support that is contained completely within the volume enclosed by a reverse helical trajectory. The cone-beam projection from the source point $\vec{r}_0(\lambda)$ can be written as

$$g(\lambda,\hat{\theta}) = \int_0^\infty dt f(\vec{r}_0(\lambda) + t\hat{\theta}), \tag{5}$$

where $\hat{\theta}$ denotes the direction of x-ray transform of $f(\vec{r})$ from $\vec{r}_0(\lambda)$. The task of image reconstruction is to recover $f(\vec{r})$ from the cone-beam projection data acquired with a reverse helical trajectory $\vec{r}_0(\lambda)$ specified in Eq. (2).

III. CHORD-BASED ALGORITHM FOR REVERSE HELICAL TRAJECTORIES

A chord of a continuous trajectory is defined as a line segment connecting any two points on the trajectory. If a volume is covered completely by chords, the image within the volume can be obtained through reconstructing images on all of the chords by use of the chord-based algorithms. Although the chord-based algorithms can have the forms of backprojection filtration (BPF)[10] and filtered backprojection (FBP),[19] we focus only on image reconstruction for a reverse helical trajectory by using the chord-based BPF algorithm in this section. Similar results can be obtained by use of the chord-based FBP algorithms.

III.A. Chord-based BPF algorithm

We consider a chord specified by λ_1 and λ_2 on a given source trajectory $\vec{r}_0(\lambda)$. Let

$$\hat{e}_c = \frac{\vec{r}_0(\lambda_2) - \vec{r}_0(\lambda_1)}{\|\vec{r}_0(\lambda_2) - \vec{r}_0(\lambda_1)\|} \tag{6}$$

denote the direction of the chord, as shown in Fig. 2. Also, we use x_c to indicate the coordinate of a point on the chord. It can be shown that the fixed coordinate and the chord coordinate of the point are related through

$$\vec{r} = \frac{1}{2}[\vec{r}_0(\lambda_1) + \vec{r}_0(\lambda_2)] + x_c\hat{e}_c, \quad x_c \in [-l,l], \tag{7}$$

where $l = 1/2\|\vec{r}_0(\lambda_2) - \vec{r}_0(\lambda_1)\|$ denotes one half of the chord length.

Using $f_c(x_c,\lambda_1,\lambda_2)$ to denote the object function on the chord, we have

$$f(\vec{r}) = f_c(x_c,\lambda_1,\lambda_2), \tag{8}$$

where $\vec{r}$ and x_c are related through Eq. (7). Because the compact support of the object function is enclosed by the trajectory, the support of the object function on a chord is finite. Without loss of generality, we assume that the object support on the chord is given by $x_c \in [x_{s1},x_{s2}]$. Considering a segment $[x_{c1},x_{c2}]$ on the chord that contains the support $x_c \in [x_{s1},x_{s2}]$, i.e., $[x_{sl},x_{s2}] \subset [x_{c1},x_{c2}]$, one has

$$f_c(x_c,\lambda_1,\lambda_2) = 0 \quad \text{for } x_c \notin [x_{s1},x_{s2}]. \tag{9}$$

From cone-beam data $g(\lambda,\hat{\theta})$, one can compute a backprojection image onto the chord as

$$g_B(x_c,\lambda_1,\lambda_2) = \int_{\lambda_1}^{\lambda_2} \frac{d\lambda}{\|\vec{r} - \vec{r}_0(\lambda)\|}\left[\frac{\partial}{\partial\lambda} g(\lambda,\hat{\theta})\right]_{\hat{\theta}}, \tag{10}$$

where $\vec{r}$ and x_c are related through Eq. (7). Based upon the backprojection image on the chord, the BPF algorithm reconstructs the object function $f_c(x_c,\lambda_1,\lambda_2)$ on the chord as

$$\begin{aligned} f_c(x_c,\lambda_1,\lambda_2) = {} & \frac{1}{2\pi^2}\frac{1}{\sqrt{(x_{c2}-x_c)(x_c-x_{c1})}} \\ & \times \left[\int_{x_{c1}}^{x_{c2}} \frac{dx_c'}{x_c - x_c'}\sqrt{(x_{c2}-x_c')(x_c'-x_{c1})}\right. \\ & \left. \times g_B(x_c',\lambda_1,\lambda_2) + C\right], \end{aligned} \tag{11}$$

where $x_c \in [x_{c1},x_{c2}]$, and the constant C is given by

$$C = 2\pi\int_{x_{c1}}^{x_{c2}} f_c(x_c,\lambda_1,\lambda_2)dx_c = 2\pi g(\lambda_1,\hat{e}_c). \tag{12}$$

III.B. Chord-based reconstructible volume

For a reverse helical trajectory, we define a one-turn trajectory segment as the portion in which the rotation direction of the source remains unchanged. The chords of a reverse helical trajectory can thus be divided into two classes: chords connecting two points within a one-turn trajectory segment, and chords connecting two points on two different one-turn trajectory segments, which we refer to as one-turn and multiple-turn chords, respectively. For a one-turn chord specified by λ_1 and λ_2, $|\lambda_1 - \lambda_2| \le 2\pi$. Therefore, a one-turn chord of a reverse helical trajectory is equivalent to the PI-line segment in a conventional helical trajectory. We display in Figs. 3(a) and 3(b) one-turn and multiple-turn chords for a two-turn reverse helical trajectory.

It has been shown that each point enclosed by the conventional helical trajectory is intersected by at least one chord, and consequently that the volume enclosed can be covered completely by chords.[16] Therefore, the image within the volume enclosed by the conventional helical trajectory can be reconstructed through reconstructing images on chords intersecting with the volume. In a reverse helical trajectory with a

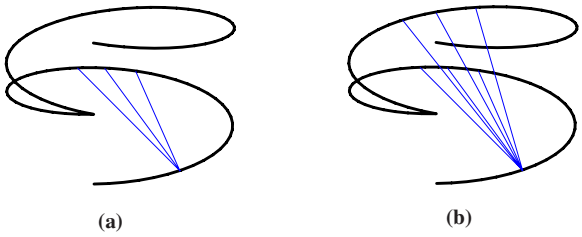

(a) (b)

FIG. 3. Illustration of chords (thin line segments) on a two-turn reverse helical trajectory (thick curve): one-turn chords (a), and multiple-turn chords (b).

finite number of turns, however, as shown in the Appendix, region(s) exist that are not intersected by any chords, and thus image(s) within the region(s) cannot be reconstructed by use of the chord-based algorithms. For a given reverse helical trajectory, one can determine the reconstructible volume by use of the chord-based algorithm through computing the volume covered by the chords. In Fig. 4, we demonstrate the volumes covered by one-turn chords and multiple-turn chords for a two-turn reverse helical trajectory, which are the reconstructible volumes by use of the chord-based algorithms. Specifically, the white regions in Fig. 4 display the reconstructible areas by use of one-turn chords (a) and multiple-turn chords (b) on the sagittal (top row), coronal (middle row), and transverse (bottom row), respectively. Clearly, regions that are not covered by any chords exist for a two-turn reverse helical trajectory; and the use of multiple-turn chords can increase the reconstructible volume.

IV. FBP ALGORITHM FOR A REVERSE HELICAL TRAJECTORY

In this section, using Pack–Noo's formula, we derive a FBP algorithm for image reconstruction from data acquired with a reversed helical trajectory.

(a) (b)

FIG. 4. Regions (white) covered by one-turn chords (a) and two-turn chords (b) within slices specified by $x=0$ (top row), $y=0$ (middle row), and $z=0$ (bottom row), respectively. Therefore, the white regions represent the reconstructible regions by use of the chord-based algorithms.

IV.A. Pack–Noo's reconstruction formula

Pack–Noo's formula provides a basis for deriving FBP algorithms for image reconstruction for a general source trajectory.[17,20] For a continuous segment of a trajectory $\vec{r}_0(\lambda)$ that begins and ends at λ^- and λ^+, we divide it into N adjacent, continuous subsegment trajectories of which the ith subsegment trajectory begins and ends at λ_i and λ_{i+1}, where $i=1,2,\ldots N$, $\lambda_1=\lambda^-$, and $\lambda_{N+1}=\lambda^+$. Therefore, $[\lambda^-,\lambda^+]=[\lambda_1,\lambda_2]\cup[\lambda_2,\lambda_3]\cup\cdots[\lambda_i,\lambda_{i+1}]\cup\cdots[\lambda_N,\lambda_{N+1}]$. For each of the subsegment trajectories, Pack–Noo's formula provides a reconstruction as

$$\mathcal{K}(\vec{r},\hat{e}_i,\lambda_i,\lambda_{i+1}) = -\frac{1}{2\pi^2}\int_{\lambda_i}^{\lambda_{i+1}} d\lambda \frac{1}{\|\vec{r}-\vec{r}_0(\lambda)\|} g_F(\lambda,\vec{r},\hat{e}_i), \tag{13}$$

where $g_F(\lambda,\vec{r},\hat{e}_i)$ represents the filtered backprojection data, given by

$$g_F(\lambda,\vec{r},\hat{e}_i) = \int_{-\pi}^{\pi} d\gamma \frac{1}{\sin\gamma} \frac{\partial g(\lambda,\hat{\theta}(\lambda,\vec{r},\hat{e}_i,\gamma))}{\partial\lambda}, \tag{14}$$

$$\hat{\theta}(\lambda,\vec{r},\hat{e}_i,\gamma) = \cos\gamma\hat{\alpha}(\lambda,\vec{r}) + \sin\gamma\hat{\beta}(\lambda,\vec{r},\hat{e}_i), \tag{15}$$

$$\hat{\beta}(\lambda,\vec{r},\hat{e}_i) = \frac{\hat{e}_i - (\hat{e}_i\cdot\hat{\alpha}(\lambda,\vec{r}))\hat{\alpha}(\lambda,\vec{r})}{\|\hat{e}_i - (\hat{e}_i\cdot\hat{\alpha}(\lambda,\vec{r}))\hat{\alpha}(\lambda,\vec{r})\|}, \tag{16}$$

and

$$\hat{\alpha}(\lambda,\vec{r}) = \frac{\vec{r}-\vec{r}_0(\lambda)}{\|\vec{r}-\vec{r}_0(\lambda)\|}. \tag{17}$$

The integration over γ in Eq. (14) indicates a filtering process over the data derivative, while the filtering direction is determined by a preselected unit vector $\hat{e}_i \in S^2$ for a subsegment trajectory specified by $[\lambda_i,\lambda_{i+1}]$. As discussed below, the specific form of a derived FBP reconstruction algorithm depends critically upon an appropriate selection of $\hat{e}_i \in S^2$.

For a given subsegment trajectory $[\lambda_i,\lambda_{i+1}]$ and a selected unit vector $\hat{e}_i$, the reconstruction term $\mathcal{K}(\vec{r},\hat{e}_i,\lambda_i,\lambda_{i+1})$, as indicated in Eq. (13), can be computed from cone-beam projections and can thus be interpreted as the known data function. Let $(R''f)(\hat{\omega},\vec{r}\cdot\hat{\omega})$ denote the second order derivative of the 3D Radon transform of the object function $f(\vec{r})$. Pack–Noo's formula[17] establishes a relationship between $\mathcal{K}(\vec{r},\hat{e}_i,\lambda_i,\lambda_{i+1})$ and $(R''f)(\hat{\omega},\vec{r}\cdot\hat{\omega})$ as

$$\mathcal{K}(\vec{r},\hat{e}_i,\lambda_i,\lambda_{i+1}) = -\frac{1}{8\pi^2}\int_{S^2} d\hat{\omega}(R''f) \times(\hat{\omega},\vec{r}\cdot\hat{\omega})\sigma(\vec{r},\hat{\omega},\hat{e}_i,\lambda_i,\lambda_{i+1}), \tag{18}$$

where

$$\sigma(\vec{r},\hat{\omega},\hat{e}_i,\lambda_i,\lambda_{i+1}) = \frac{1}{2}\,\mathrm{sgn}(\hat{\omega}\cdot\hat{e}_i)[\mathrm{sgn}(\hat{\omega}\cdot\hat{\alpha}(\lambda_i,\vec{r})) - \mathrm{sgn}(\hat{\omega}\cdot\hat{\alpha}(\lambda_{i+1},\vec{r}))] \tag{19}$$

and "sgn" denotes the signum function. Therefore, for the N

continuous subsegment trajectories covering the entire trajectory $\lambda \in [\lambda^-, \lambda^+]$, we have

$$\sum_{i=1}^{N} \mathcal{K}(\vec{r}, \hat{e}_i, \lambda_i, \lambda_{i+1}) = -\frac{1}{8\pi^2} \int_{S^2} d\hat{\omega} (R''f) \times (\hat{\omega}, \vec{r} \cdot \hat{\omega}) \overline{\sigma}(\vec{r}, \hat{\omega}, \lambda^-, \lambda^+), \quad (20)$$

where

$$\overline{\sigma}(\vec{r}, \hat{\omega}, \lambda^-, \lambda^+) = \sum_{i=1}^{N} \sigma(\vec{r}, \hat{\omega}, \hat{e}_i, \lambda_i, \lambda_{i+1}). \quad (21)$$

It can be observed that, if the weighting function

$$\overline{\sigma}(\vec{r}, \hat{\omega}, \lambda^-, \lambda^+) = P = \text{const.}, \quad (22)$$

the right-hand side of Eq. (20) yields exactly P times the inverse 3D radon transform of the object function. Under the condition in Eq. (22), the object function $f(\vec{r})$ is obtained as

$$f(\vec{x}) = \frac{1}{P} \sum_{i=1}^{N} \mathcal{K}(\vec{r}, \hat{e}_i, \lambda_i, \lambda_{i+1}). \quad (23)$$

The result in Eq. (23) is referred to as the FBP reconstruction algorithm, and its derivation, as discussed above, depends upon the appropriate selection of the unit vectors $\{\hat{e}_i\}$ for determining the filtering directions and upon the calculation of $\{\mathcal{K}(\vec{r}, \hat{e}_i, \lambda_i, \lambda_{i+1})\}$.

IV.B. The FBP algorithm for reverse helical trajectories

Using Pack–Noo's formula, we derive below a FBP algorithm for image reconstruction from cone-beam data acquired with a two-turn reverse helical trajectory. Extension of the derived algorithm to multiple-turn reverse helical trajectories is straightforward and will be briefly described.

For a continuous scanning trajectory, one can define a polygon plane as the plane that intersects the trajectory at more than two points. For each side of a polygon, there exists a continuous subsegment of the source trajectory connecting two ends of the side of the polygon. Based on Pack–Noo's formula, a polygon-based FBP algorithm has been developed for image reconstruction for circular sinusoidal trajectories, including the saddle trajectory.[18] For a circular sinusoidal trajectory, without loss of generality, we consider a polygon of four sides that intersects the trajectory four times. Let unit vectors $\hat{e}_i$ denote the directions of the polygon sides, i.e.,

$$\hat{e}_i = \frac{\vec{r}_0(\lambda_{i+1}) - \vec{r}_0(\lambda_i)}{\|\vec{r}_0(\lambda_{i+1}) - \vec{r}_0(\lambda_i)\|}, \quad (24)$$

where λ_i and λ_{i+1} denote the starting and ending points of the ith subsegment trajectory corresponding to the ith side of the polygon, and $i=1,2,3$, and 4. In this case, it has been shown[18,21] that

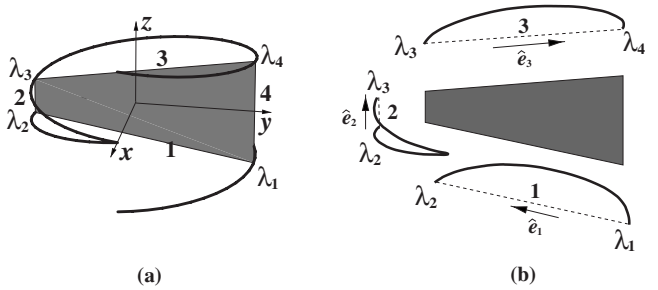

FIG. 5. (a) The four-side polygon (shaded region) formed by four chords each of which connects two points on the two-turn reverse helical trajectory. The polygon plane is chosen to be parallel to y-z plane. (b) Continuous subsegment trajectories (thick curves) corresponding to sides i of the four-side polygon (dashed lines), and the directions $\hat{e}_i$ of the chords (i.e., the sides) of the polygon, where $i=1,2$, and 3.

$$\overline{\sigma}(\vec{r}, \hat{\omega}, \lambda^-, \lambda^+) = \sum_{i=1}^{4} \sigma(\vec{r}, \hat{\omega}, \hat{e}_i, \lambda_i, \lambda_{i+1}) = 2, \quad (25)$$

where $\lambda^- = \lambda_1$, $\lambda^+ = \lambda_5$, and $\vec{r}_0(\lambda^+) = \vec{r}_0(\lambda^-)$. Using this result in Eq. (23), one obtains the FBP algorithm for exact image reconstruction within the polygon, which is written as

$$f(\vec{r}) = \frac{1}{2} \sum_{i=1}^{4} \mathcal{K}(\vec{r}, \hat{e}_i, \lambda_i, \lambda_{i+1}). \quad (26)$$

We now extend the FBP algorithm above to reconstruct images for a two-turn reverse helical trajectory depicted in Fig. 5. First of all, it is important to observe, for a given point $\vec{r}$ within and the side direction $\hat{e}_i$ of the polygon, that both $\sigma(\vec{r}, \hat{\omega}, \hat{e}_i, \lambda_i, \lambda_{i+1})$ and $\mathcal{K}(\vec{r}, \hat{e}_i, \lambda_i, \lambda_{i+1})$ depend only upon the starting and ending points λ_i and λ_{i+1}, while being independent of the shape of the continuous subsegment trajectory corresponding to side i of the polygon. Therefore, the results in Eqs. (25) and (26) are directly applicable to image reconstruction within a four-side polygon defined on a general trajectory, under the conditions that (1) $\lambda^- = \lambda_1$, $\lambda^+ = \lambda_5$, and $\vec{r}_0(\lambda^+) = \vec{r}_0(\lambda^-)$ and (2) each side of the polygon has a continuous subsegment trajectory connecting the two ends of the side.

Consider a polygon plane in Fig. 5(a) that is parallel to the y-z plane and that intersects the reverse helical trajectory at four distinctive points $\vec{r}_0(\lambda_i)$, where $i=1,\ldots,4$; and $-2\pi \leq \lambda_1 < \lambda_2 \cdots < \lambda_4 \leq 2\pi$. It can be observed in Fig. 5(b) that each of sides 1, 2, and 3 of the polygon has a distinct, continuous subsegment trajectory connecting its two ends. However, side four of the polygon has a distinct, discontinuous subsegment trajectory, which contains the starting and ending points λ_s and λ_e of the reverse helical trajectory, as displayed in Fig. 6(a). Therefore, Eq. (26) cannot directly be applied to reconstructing an exact image within the polygon for the reverse helical trajectory.

A continuous subsegment trajectory for side four may be formed through including an additional continuous subsegment trajectory that connects the starting point λ_s and the ending point λ_e of the two-turn reverse helical trajectory. For example, a continuous subsegment trajectory passing λ_s and

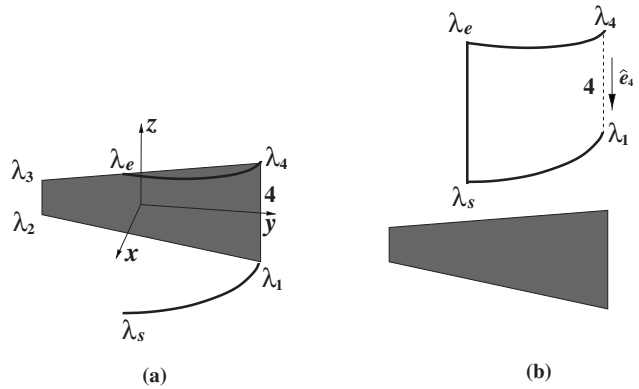

FIG. 6. (a) For side four of the polygon (shade region), the subsegment trajectory containing the starting and ending points λ_s and λ_e consists of two discontinuous segments (thick curves). (b) A continuous subsegment trajectory passing λ_s and λ_e can be formed for side four through including, e.g., an additional, straight subsegment trajectory connecting λ_s and λ_e. Again, $\hat{e}_4$ denotes the direction of side four (dashed line) of the polygon.

λ_e is formed in Fig. 6(b), which includes an additional, straight subsegment trajectory connecting λ_s and λ_e. However, an additional subsegment trajectory requires an additional scan, thus resulting in additional scanning effort and radiation dose.

It is indeed possible to identify a continuous subsegment trajectory for side four without involving any additional scan to the reverse helical trajectory.[22] As shown in Fig. 7, the union of the three distinct subsegment trajectories corresponding to sides 1, 2, and 3 of the polygon forms a continuous subsegment trajectory for side four of the polygon. As mentioned above, $\mathcal{K}(\vec{r},\hat{e}_4,\lambda_4,\lambda_5)$ is independent of the shape of the continuous subsegment trajectory, while depending only upon λ_4 and λ_5, where λ_5 satisfies $\vec{r}_0(\lambda_5)=\vec{r}_0(\lambda_1)$. Therefore, we can use the union of three distinct subsegment trajectories of sides 1, 2, and 3 to compute $\mathcal{K}(\vec{r},\hat{e}_4,\lambda_4,\lambda_5)$. In fact, from Eq. (5) and Eqs. (13)–(17), it can be seen that $\mathcal{K}(\vec{r},\hat{e}_i,\lambda_i,\lambda_{i+1})$ depends upon λ_i and λ_{i+1} through $\vec{r}_0(\lambda_i)$ and $\vec{r}_0(\lambda_{i+1})$. Therefore,

$$\mathcal{K}(\vec{r},\hat{e}_4,\lambda_4,\lambda_5)=\mathcal{K}(\vec{r},\hat{e}_4,\lambda_4,\lambda_1), \tag{27}$$

in which we have used $\vec{r}_0(\lambda_5)=\vec{r}_0(\lambda_1)$. Furthermore, using Eq. (13), one can readily show that

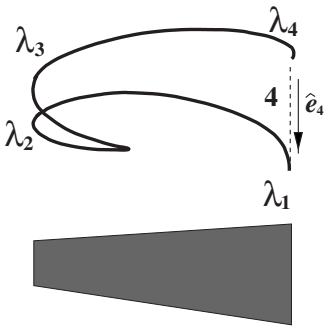

FIG. 7. The portion of a two-turn reverse helical trajectory passing through λ_2 and λ_3 forms a continuous subsegment trajectory for side four of the polygon in Fig. 5.

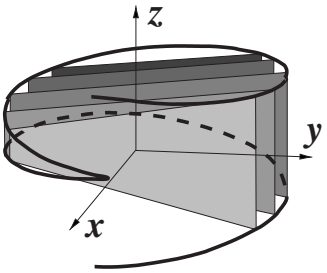

FIG. 8. The volume enclosed by a two-turn reverse helical trajectory can be decomposed into a set of parallel polygons. Without loss of generality, a set of polygons parallel to *y*-*z* plane is shown. A volume image can be obtained through reconstructing images within the polygons by use of the proposed FBP algorithm.

$$\mathcal{K}(\vec{r},\hat{e}_i,\lambda_4,\lambda_1)=-\mathcal{K}(\vec{r},\hat{e}_i,\lambda_1,\lambda_4). \tag{28}$$

Finally, an exact image reconstruction within the polygon for a two-turn reverse helical trajectory can be obtained as

$$f(\vec{r})=\frac{1}{2}\sum_{i=1}^{4}\mathcal{K}(\vec{r},\hat{e}_i,\lambda_i,\lambda_{i+1})=\frac{1}{2}\sum_{i=1}^{3}\mathcal{K}(\vec{r},\hat{e}_i,\lambda_i,\lambda_{i+1})-\frac{1}{2}\mathcal{K}(\vec{r},\hat{e}_4,\lambda_1,\lambda_4). \tag{29}$$

We refer to Eq. (29) as the FBP algorithm for image reconstruction for a reverse helical trajectory. As shown in Fig. 8, the volume enclosed by a reverse helical trajectory can be decomposed into a set of polygons. Therefore, one can achieve a volume-image reconstruction for a reverse helical trajectory through reconstructing images within the set of polygons by use of the FBP algorithm described.

The FBP algorithm above was derived for a two-turn reverse helical trajectory. Similar approach can readily be applied to deriving an FBP algorithm for multiple-turn reverse helical trajectories. Without loss of generality, we use a three-turn reverse helical trajectory to illustrate such an extension. Again, for the given reverse helical trajectory, we first select a four-side polygon whose four corners reside on the trajectory, as shown in Fig. 9. In the case of a multiple-turn reverse helical trajectory, different polygons can be devised. In Figs. 9(a) and 9(b), two different four-side polygons are displayed. In these cases, it can be readily shown that,

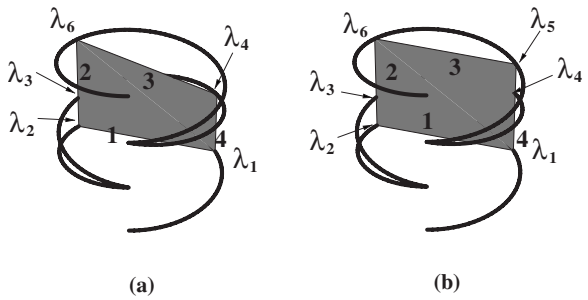

FIG. 9. (a) A polygon with four corners intersecting the three-turn reverse helical trajectory at λ_1, λ_2, λ_4, and λ_6. (b) A polygon with four corners intersecting the three-turn reverse helical trajectory at λ_1, λ_2, λ_5, and λ_6.

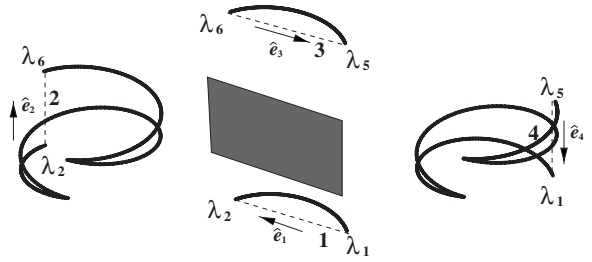

FIG. 10. The continuous subsegment trajectories corresponding to each side of the polygon in Fig. 9(b).

when unit vectors $\{\hat{e}_i\}$ are selected along each of the sides of the polygon, the result in Eq. (25) remains unchanged. Furthermore, a continuous subsegment trajectory can be identified for each side of the polygon. In Fig. 10, we display the continuous subsegment trajectories for each side of the polygon in Fig. 9(b). From these continuous subsegment trajectories, one can compute $\mathcal{K}(\vec{r},\hat{e}_i,\lambda_i,\lambda_{i+1})$ and use them in Eq. (29) to obtain the image within the polygon. Finally, one can obtain a volume image by reconstructing 2D images within a set of polygons in the volume enclosed by the reverse helical trajectories, as displayed in Fig. 11.

V. NUMERICAL RESULTS

We have performed computer simulation studies to validate that the proposed FBP algorithm can reconstruct images within the volume enclosed by a reverse helical trajectory, including the chordless regions that cannot be reconstructed by use of the chord-based algorithm. A low contrast 3D Shepp–Logan phantom was used that has an ellipsoid support with axes of 13.8, 18.0, and 18.4 cm along the *x*, *y*, and *z* axis, respectively. Additionally, a high contrast shoulder phantom was also used that has an ellipsoid support with axes of 16.0, 8.0, and 8.0 cm along the *x*, *y*, and *z* axis, respectively. The shoulder phantom has been designed specifically to supply *z*-slice images that look like FORBILD thorax phantom and also to prevent data truncation for this study.[23] The details of the shoulder phantom are described in Table I. In the phantom, different types of objects are included: cut ellipsoid (CE) that has cuts along long axis, ellipsoid (E), cone (CN), and cylinder (CL). Parameters represent half lengths of long axis and two other short axes for CE and E; top radius, bottom radius, and height for CN; and radius and height for CL. Polar (θ) and azimuthal (ϕ) angles are given in degrees. All the lengths are in relative units, and the phantom has been resized in the numerical study. The reverse helical trajectories have radii of $R=60$ cm and the distances of $D=75$ cm from the sources to detectors. The number of projections per turn is 800. We used helical pitch of $h=40$ cm in the simulation study for the proposed FBP algorithm. For the purpose of clearly demonstrating the chordless region in the reconstruction, we used a helical

TABLE I. Shoulder phantom description.

Type	Center	Parameters	Cut-length	Angles (θ,ϕ)	Density
CE	0,0,0	80,40,40	−70,70	0,0	1.5
CE	−80,0,0	22,22,22	−22,10	0,0	1.5
CE	80,0,0	22,22,22	−10,22	0,0	1.5
E	−88,0,0	10,10,10		0,0	2.3
E	−88,0,0	8,8,8		0,0	1.5
E	88,0,0	10,10,10		0,0	2.3
E	88,0,0	8,8,8		0,0	1.5
E	−65,0,0	10,10,10		0,0	2.3
E	−65,0,0	8,8,8		0,0	1.5
E	65,0,0	10,10,10		0,0	2.3
E	65,0,0	8,8,8		0,0	1.5
E	0,20,0	5,5,5		0,0	2.3
CE	0,20,0	6.5,6.5,6.5	−5.5,6.5	0,−90	3.0
CN	0,27.5,0	3.5,15,4		0,0	3.0
CL	0,33,0	1.5,7		90,90	3.0
E	−40,20,0	23,3,3		0,20	2.3
E	−40,20,0	18,2,2		0,20	1.5
E	40,20,0	23,3,3		0,−20	2.3
E	40,20,0	18,2,2		0,−20	1.5
CL	0,−36,0	2,9		90,0	2.3
CL	0,−36,0	1,7		90,0	1.5
CE	12,−35,0	13,2,2	−1,13	0,20	2.3
CE	12,−35,0	10,1,1	0,10	0,20	1.5
CE	−12,−35,0	13,2,2	−13,1	0,−20	2.3
CE	−12,−35,0	10,1,1	−10,0	0,−20	1.5
E	−20,5,0	4,5,5		0,0	2.0
E	−10,−15,0	13,15,10		0,−30	2.0
E	20,5,0	12,10,10		0,30	2.0

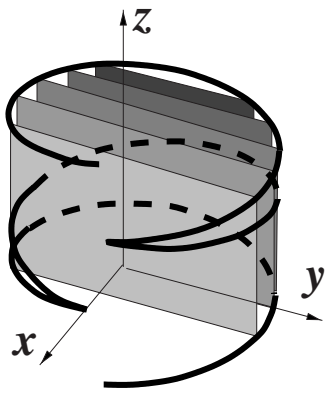

FIG. 11. The volume enclosed by a three-turn reverse helical trajectory can be decomposed into a set of parallel polygons. A set of polygons parallel to *y*-*z* plane is shown here. A volume image can be obtained through reconstructing images within the polygons.

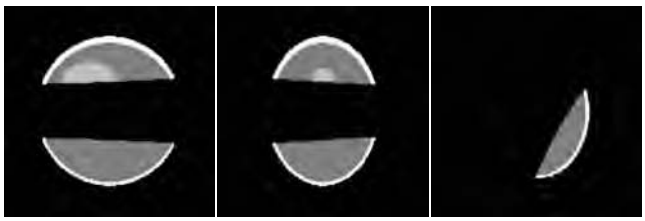

FIG. 12. Images of the Shepp–Logan phantom within slices at (a) $x=0$ cm, (b) $y=0$ cm, and (c) $z=-2.5$ cm reconstructed from noiseless data by use of the chord-based algorithm on one-turn chords. Display window is [1.0,1.04].

FIG. 13. Images of the Shepp–Logan phantom within slices at (a) $x=0$ cm, (b) $y=0$ cm, and (c) $z=-2.5$ cm reconstructed from noiseless data by use of the chord-based algorithm on both one-turn and two-turn chords. Display window is [1.0,1.04].

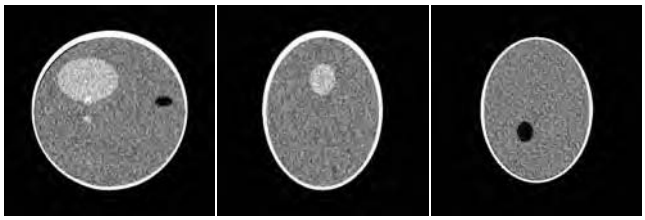

FIG. 15. Images of the Shepp–Logan phantom within slices at (a) $x=0$ cm, (b) $y=0$ cm, and (c) $z=-2.5$ cm reconstructed from the noisy data by use of the proposed FBP algorithm. Display window is [1.01,1.03].

pitch of $h=15$ cm in the simulation study involving the chord-based BPF algorithm. When $h=40$ cm is used for the chord-based BPF algorithm study, the phantom would be barely reconstructed that the difference between the images, reconstructed by use of only one-turn chords and two-turn chords as well, is small. The detector panel considered here has an effective square area that consists of 400×400 pixels each of which has a size of 0.78×0.78 mm^2. Image reconstruction volume consists of $400\times400\times400$ voxels each of which has a size of $0.61\times0.61\times0.61$ mm^3. Similar discretization rules to those in Ref. 21 have been used in the implementation of the algorithm, which are summarized in the Appendix B.

In Figs. 12 and 13, we display images of the Shepp–Logan phantom within slices at (a) $x=0$ cm, (b) $y=0$ cm, and (c) $z=-2.5$ cm reconstructed on one-turn and multiple-turn chords by using the chord-based BPF algorithm. Clearly, the BPF algorithm can accurately reconstruct images within the regions covered the chords. Comparison of the reconstructive regions in Figs. 12 and 13 indicates that the use of multiple-turn chords leads to a larger reconstructible region than that only from the one-turn chords. However, it can also be observed in both cases that the BPF algorithm cannot yield images within the chordless regions (e.g., the dark regions between the two reconstructible regions).

In Fig. 14, we show images of the Shepp–Logan phantom within slices at (a) $x=0$ cm, (b) $y=0$ cm, and (c) $z=-2.5$ cm reconstructed by using the proposed FBP algorithm. The results indicate that the proposed algorithm can reconstruct an image within the volume enclosed by a reverse helical trajectory. In an attempt to demonstrate quantitatively the reconstruction accuracy, we display in Fig. 14(d) the profile along a vertical line, specified by $x=0$ cm and $y=-2.5$ cm, passing through the Shepp–Logan phantom, as indicated in Fig. 14(a). For comparison, we also plot the corresponding true profile as dotted curve in Fig. 14(d). The profile results suggest that the proposed FBP algorithm can accurately reconstruct an image within the entire volume enclosed by the reverse helical trajectory. We have also performed a preliminary reconstruction from noisy data by use of the proposed FBP algorithm. We included Gaussian noise in the projection data with the noise level of 0.25%. From the noisy data, we reconstructed images by use of the proposed FBP algorithm. In Fig. 15, we display the reconstructed noisy images within slices at (a) $x=0$ cm, (b) $y=0$ cm, and (c) $z=-2.5$ cm.

In Fig. 16, we show images of the shoulder phantom within slices at (a) $x=0$ cm, (b) $y=0$ cm, and (c) $z=0$ cm reconstructed by using the proposed FBP algorithm. We also display in Fig. 16(d) the profile along a horizontal line, specified by $y=0.5$ cm and $z=0$ cm, passing through the phantom, as indicated in Fig. 16(c). Corresponding true profile is represented by a dotted curve in Fig. 16(d). These results indicate the proposed algorithm can reconstruct high contrast variations accurately as well although some image artifacts due to discretization errors are observable such as streaks in Fig. 16(c). We included Gaussian noise in the projection data with the noise level of 1.0%. From the noisy data, we reconstructed images by use of the proposed FBP algorithm. In Fig. 17, we display the reconstructed noisy images within slices at (a) $x=0$ cm, (b) $y=0$ cm, and (c) $z=0$ cm.

VI. DISCUSSION

In the work, we have proposed reverse helical trajectories for acquiring cone-beam data, and have investigated and de-

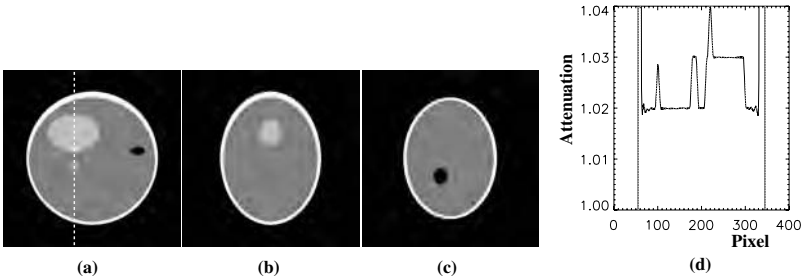

FIG. 14. Images of the Shepp–Logan phantom within slices at (a) $x=0$ cm, (b) $y=0$ cm, and (c) $z=-2.5$ cm reconstructed from noiseless data by use of the proposed FBP algorithm. Display window is [1.0,1.04]. (d) Profile on the vertical line specified by $x=0$ cm and $y=-2.5$ cm, which is also indicated in (a). The reconstructed and true profiles are displayed as solid and dotted curves, respectively.

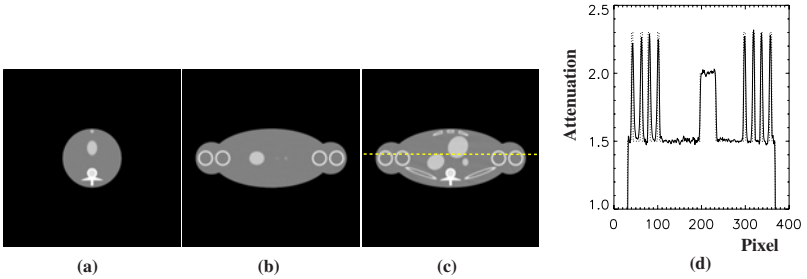

FIG. 16. Images of the shoulder phantom within slices at (a) $x=0$ cm, (b) $y=0$ cm, and (c) $z=0$ cm reconstructed from noiseless data by use of the proposed FBP algorithm. Display window is [1.0,2.5]. (d) Profile on the horizontal line specified by $y=0.5$ cm and $z=0$ cm, which is also indicated in (c). The reconstructed and true profiles are displayed as solid and dotted curves, respectively.

veloped algorithms for image reconstruction from such cone-beam data. The proposed reverse helical trajectories and reconstruction algorithms may find use in IGRT and other applications. Recently, chord-based algorithms such as the BPF algorithm have been developed for image reconstruction from data acquired with general trajectories, provided that the trajectories have chords covering the object. However, reverse helical trajectories are unique in that, although they satisfy Tuy's sufficient data condition for nontruncated object, certain parts of the volume enclosed by them are not covered by chords. Consequently, the chord-based algorithms cannot reconstruct images within the chordless regions of reverse helical trajectories. For a given reverse helical trajectory, we have investigated its chordless regions; and we then conducted image reconstruction by use of the chord-based BPF algorithm to demonstrate the nonreconstructible, chordless regions.

As mentioned above, however, the volume enclosed by a reverse helical trajectory satisfies Tuy's condition, suggesting that exact image of an object within the reverse helix volume including the chordless regions can be reconstructed. We have proposed a FBP algorithm based on Pack–Noo's formula to reconstruct the images within the volume enclosed by a reverse helical trajectory, thus eliminating the chordless region that is nonreconstructible by use of the chord-based algorithms. Numerical studies were also conducted to validate the proposed FBP algorithm. Results of the numerical studies confirm that, unlike the chord-based algorithm, the proposed FBP algorithm can reconstruct an accurate image for the entire reverse helix volume. Since the proposed algorithm is of FBP type, it is in general computationally efficient. However, data filtering has to be performed at least twice for each projection, which may increase the amount of computation compared to a conventional FBP algorithm.

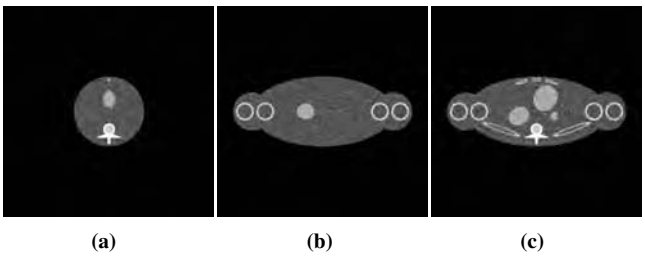

FIG. 17. Images of the shoulder phantom within slices at (a) $x=0$ cm, (b) $y=0$ cm, and (c) $z=0$ cm reconstructed from the noisy data by use of the proposed FBP algorithm. Display window is [1.0,2.5].

Interestingly, the developed FBP algorithm allows certain transverse data truncation. This is because the data filtering is determined only by the directions of the polygon sides within which the image is to be reconstructed. When the polygons covering the reverse helix volume are selected to be, e.g., parallel to the y-z plane, as we did here, data truncation along the x axis outside the volume covered by the polygons does not affect the image-reconstruction accuracy within these polygons. However, the proposed FBP algorithm generally allows no truncation longitudinally and is thus incapable of dealing with a long object problem. For a reverse helical trajectory with a long object problem, we are developing a combined image-reconstruction method in which the chord-based algorithm is used for addressing the long object problem, and the proposed FBP algorithm is used for dealing with image reconstruction within the chordless regions. The research of this combined method is beyond the scope of the current work and will be reported elsewhere in the future. We have also discussed the extension of the proposed FBP algorithm to reconstruct images for multiple-turn reverse helical trajectories. In fact, it should be pointed out that the proposed FBP algorithm can readily be generalized to address the problems of image reconstruction for reverse helical trajectories with tilted axis, or variable pitches, or additional scanning trajectory segments.

ACKNOWLEDGMENTS

S.C. is supported in part by DOD Predoctoral training Grant No. PC061210, and D.X. is supported in part by DOD Predoctoral training Grant No. BC051553. This work was also supported in part by National Institutes of Health Grant Nos. EB00225 and CA120540. Its contents are solely the responsibility of the authors and do not necessarily represent the official views of the National Institutes of Health. The authors would like to thank Dr. Yu Zou for his help on shoulder phantom.

APPENDIX A: ANALYSIS OF THE CHORDLESS REGIONS IN A REVERSE HELICAL TRAJECTORY

It is shown here that there exist chordless regions in the volume enclosed by a two-turn reverse helical trajectory. For simplifying the discussion, we consider intersecting points along z axis, which is the rotation axis, with all the possible chords, and we show that there exists a region between intersecting regions on z axis. A chord passing through z axis defines a unique plane containing the chord and z axis. For a

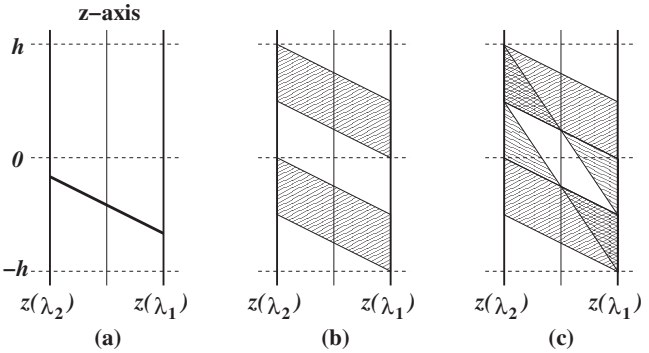

FIG. 18. Diagrams demonstrating the chordless region along z axis for a two-turn reverse helical trajectory. (a) An exemplary chord plotted on the plane defined by the chord and z axis. (b) Collection of all one-turn chords. (c) Collection of all chords including multiple-turn chords.

given chord passing through z axis, we label the angular parameter of the lower end by λ_1 and that of the upper end by λ_2. A chord, for example, is presented on the defined plane in Fig. 18. Using circular symmetry, we can establish the functional relationship, as summarized in Table II, between $z(\lambda_1)$ and $z(\lambda_2)$ for one-turn chords and also for multiple-turn chords, where $z(\lambda)$ indicates the z coordinate of a source point on the reverse helical trajectory at λ. The z-coordinate, $z_0(\lambda_1,\lambda_2)$, of the intersecting point of a chord withz axis is given by

$$z_0(\lambda_1,\lambda_2)=\frac{1}{2}[z(\lambda_1)+z(\lambda_2)], \tag{A1}$$

which is in the shaded regions in Figs. 18(a) and 18(b) for one-turn and multiple-turn chords. The chordless (white) region can be observed between the intersecting (shaded) regions.

APPENDIX B: IMPLEMENTATION OF THE PROPOSED FBP ALGORITHM

For discussion of algorithm implementation, we introduce a rotation-coordinate system $\{u,v,w\}$ in which its origin is on the source $\vec{r}_0(\lambda)$, and its u-w plane and v axis are parallel to the x-y plane and to the z axis, respectively, of the fixed-coordinate system $\{x,y,z\}$. The unit vectors of the rotation-coordinate system at a scanning angle λ can be expressed in the fixed-coordinate system as

$$\hat{e}_u(\lambda)=(-\sin\lambda,\cos\lambda,0)$$

$$\hat{e}_v(\lambda)=(0,0,1)$$

$$\hat{e}_w(\lambda)=(\cos\lambda,\sin\lambda,0). \tag{B1}$$

Let the flat-panel detector be placed within a plane at $w=-D$ that is parallel to the u-v plane. We introduce a 2D-detector-coordinate system $\{u_d,v_d\}$ on the plane in which the u_d and v_d axes are parallel to the u and v axes, respectively, and its origin is at the projection, along $\hat{e}_w$, on the detector plane, of the source point $\vec{r}_0(\lambda)$. For a point $\vec{x}_d$ on the detector plane, the relationship between its fixed coordinates (x_d,y_d,z_d) and 2D-detector coordinates (u_d,v_d) can be obtained as

$$x_d=-u_d\sin\lambda+(-D+R)\cos\lambda$$

$$y_d=u_d\cos\lambda+(-D+R)\sin\lambda$$

$$z_d=v_d+\frac{h}{2\pi}\lambda. \tag{B2}$$

Now the three steps of the algorithm can be summarized as follows.

Data derivative: We compute

$$\frac{\partial g(\lambda,\hat{\theta})}{\partial\lambda}=\frac{\partial g(\lambda,u_d,v_d)}{\partial\lambda}=\left(\frac{\partial}{\partial\lambda}+\frac{D^2+u_d^2}{D}\frac{\partial}{\partial u_d}+\frac{u_dv_d}{D}\frac{\partial}{\partial v_d}\right)g(\lambda,u_d,v_d). \tag{B3}$$

Three points differentiation method has been used for computing derivatives.

Hilbert transform: For given filtering direction $\hat{e}$, we compute 1D Hilbert transform along the projection of $\hat{e}$ at image point $\vec{r}$ onto the detector as

$$g_F(\lambda,\vec{r},\hat{e})=g_F(\lambda,u_d,v_d,\hat{e})=\int_{u_l}^{u_u}du_d'\frac{A}{A'}h_H(u_d-u_d')\frac{\partial g(\lambda,u_d',v_d')}{\partial\lambda}, \tag{B4}$$

where $h_H(u)$ is the kernel of Hilbert transform, $A=\sqrt{D^2+u_d^2+v_d^2}$, and $A'=\sqrt{D^2+u_d'^2+v_d'^2}$. Upper and lower integration boundaries can be either $(-\infty,\infty)$ or $(\infty,-\infty)$ depending on the relative position $\vec{r}_0(\lambda)$ with respect to the reconstruction point $\vec{r}$. Rebinning and back-rebinning method similar to that used in Ref. 21 has been used for integration.

Backprojection: We compute

TABLE II. Relationship between the z coordinates of chords passing through z axis for a two-turn reverse helical trajectory.

	λ_1	$-2\pi\le\lambda_1\le-\pi$	$-\pi<\lambda_1<0$	$0\le\lambda_1\le\pi$	$\pi<\lambda_1\le2\pi$
	$z(\lambda_1)$	$h/2\pi(\lambda_1)$	$h/2\pi(\lambda_1)$	$h/2\pi(\lambda_1)$	$h/2\pi(\lambda_1)$
One-turn chords	$z(\lambda_1)$	$h/2\pi(\lambda_1+\pi)$	None	$h/2\pi(\lambda_1+\pi)$	None
Multiple-turn chords	$z(\lambda_2)$	$h/2\pi(-\lambda_1-\pi)$	$h/2\pi(-\lambda_1+\pi)$	None	None

$$\mathcal{K}(\vec{r},\hat{e}_i,\lambda_i,\lambda_{i+1}) = -\frac{1}{2\pi^2}\int_{\lambda_i}^{\lambda_{i+1}} d\lambda \frac{1}{\|\vec{r}-\vec{r}_0(\lambda)\|} g_F(\lambda,\vec{r},\hat{e}_i). \tag{B5}$$

Bilinear interpolation has been used for computing the backprojection.

[a]Author to whom correspondence should be addressed. Electronic mail: xpan@uchicago.edu

[1]D. A. Jaffray and J. H. Siewerdsen, "Cone-beam computed tomography with a flat-panel imager: Initial performance characterization," Med. Phys. **27**, 1311–1323 (2000).
[2]J. H. Siewerdsen and D. A. Jaffray, "Optimization of x-ray imaging geometry (with specific application to flat-panel cone-beam computed tomography)," Med. Phys. **27**, 1903–1914 (2000).
[3]B. A. Groh, J. H. Siewerdsen, D. G. Drake, J. W. Wong, and D. A. Jaffray, "A performance comparison of flat-panel imager-based MV and kV cone-beam CT," Med. Phys. **29**, 967–975 (2002).
[4]L. A. Feldkamp, L. C. Davis, and J. W. Kress, "Practical cone-beam algorithm," J. Opt. Soc. Am. **A1**, 612–619 (1984).
[5]S. Mori, M. Endo, S. Komatsu, S. Kandatsu, T. Yashiro, and M. Baba, "A combination-weighted Feldkamp-based reconstruction algorithm for cone-beam CT," Phys. Med. Biol. **51**, 3953–3965 (2006).
[6]S. Valton, F. Peyrin, and D. Sappey-Marinier, "Analysis of cone-beam artifacts in off-centered circular CT for four reconstruction methods," Int. J. Biomed. Imaging **2006**, 1–8 (2006).
[7]S. Yoo and F. Yin, "TU-FF-A2-01: Feasibility of cone-beam CT based treatment planning," Med. Phys. **33**, 2219 (2006).
[8]A. Katsevich, "Theoretically exact FBP-type inversion algorithm for spiral CT," SIAM J. Appl. Math. **62**, 2012–2026 (2002).
[9]F. Noo, J. Pack, and D. Heuscher, "Exact helical reconstruction using native cone-beam geometries," Phys. Med. Biol. **48**, 3787–3818 (2003).
[10]Y. Zou and X. Pan, "Exact image reconstruction on PI-line from minimum data in helical cone-beam CT," Phys. Med. Biol. **49**, 941–959 (2004).
[11]Y. Ye and G. Wang, "Filtered backprojection formula for exact image reconstruction from cone-beam data along a general scanning curve," Med. Phys. **32**, 654–665 (2005).
[12]J. D. Pack, F. Noo, and R. Clackdoyle, "Cone-beam reconstruction using the backprojection of locally filtered projections," IEEE Trans. Med. Imaging **24**, 2317–2336 (2005).
[13]Y. Zou, X. Pan, and E. Y. Sidky, "Theory and algorithms for image reconstruction on chords and within regions of interest," J. Opt. Soc. Am. **22**, 2372–2384 (2005).
[14]A. Katsevich, "Image reconstruction for the circle-arc trajectory," Phys. Med. Biol. **50**, 2249–2265 (2005).
[15]T. Zhuang and G. Chen, "New families of exact fan-beam and cone-beam image reconstruction formulae via filtering the backprojection image of differentiated projection data along singly measured lines," Inverse Probl. **22**, 991–1006 (2006).
[16]P. E. Danielsson, P. Edholm, and M. Seger, "Towards exact 3D-reconstruction for helical cone-beam scanning of long objects. A new detector arrangement and a new completeness condition," in *Proceedings of the 1997 International Meeting on Fully Three-Dimensional Image Reconstruction in Radiology and Nuclear Medicine*, edited by D. W. Townsend and P. E. Kinahan, Pittsburgh, 1997.
[17]J. D. Pack and F. Noo, "Cone-beam reconstruction using 1D filtering along the projection of M-lines," Inverse Probl. **21**, 1105–1120 (2005).
[18]H. Yang, M. Li, K. Koizumi, and H. Kudo, "Application of Pack and Noo's cone-beam inversion formula to a wide class of trajectories," in *IEEE Medical Imaging Conference Record*, San Diego, CA, 2006, pp. M14–450.
[19]E. Y. Sidky, Y. Zou, and X. Pan, "Minimum data image reconstruction algorithms with shift-invariant filtering for helical, cone-beam CT," Phys. Med. Biol. **50**, 1643–1657 (2005).
[20]J. D. Pack and F. Noo, "Cone-beam reconstruction outside R-lines using the backprojection of 1-D filtered data," in *Proceedings of the 2005 International Meeting on Fully Three-Dimensional Image Reconstruction in Radiology and Nuclear Medicine*, Salt Lake City, UT, pp. 287–290 (2005).
[21]H. Yang, M. Li, K. Koizumi, and H. Kudo, "Exact cone beam reconstruction for a saddle trajectory," Phys. Med. Biol. **51**, 1157–1172 (2006).
[22]D. Xia, S. Cho, and X. Pan, "Image reconstruction for cone-beam CT with reduced-scan circular sinusoidal trajectories," IEEE Trans. Med. Imaging (submitted).
[23]http://www.imp.uni erlangen.de/phantoms/thorax/thorax.htm

Region-Of-Interest Image Reconstruction with Intensity-Weighting in Circular Cone-Beam CT for Image-Guided Radiation Therapy

[1,2]Seungryong Cho, [2]Erik Pearson,[2]Charles A. Pelizzari, [1]Xiaochuan Pan
[1]Department of Radiology, University of Chicago, Chicago, IL 60637
[2]Department of Radiation and Cellular Oncology, University of Chicago, Chicago, IL 60637

Abstract

Imaging plays a vital role in radiation therapy and with recent advances in technology considerable emphasis has been placed on cone-beam CT (CBCT). Attaching a kV x-ray source and flat panel detector directly to the linear accelerator gantry has enabled progress in target localization techniques, which can include daily CBCT set-up scans for some treatments. However, with an increasing number of CT scans there is also an increasing concern for patient exposure. An intensity-weighted region-of-interest (IWROI) technique, which has the potential to greatly reduce CBCT dose, in conjunction with the chord-based backprojection-filtration (BPF) reconstruction algorithm has been developed and its feasibility in clinical use is demonstrated in this paper. A nonuniform filter is placed in the x-ray beam to create regions of two different beam intensities. In this manner, regions outside the target area can be given a reduced dose but still visualized with a lower contrast-to-noise-ratio (CNR). Image artifacts due to transverse data truncation, which would have occurred in conventional reconstruction algorithms, are avoided and image noise levels of the low and high-intensity regions are well controlled by use of the chord-based BPF reconstruction algorithm. The proposed IWROI technique can play an important role in image-guided radiation therapy (IGRT).

1 Introduction

Cone-beam CT (CBCT) is widely used in image-guided radiation therapy (IGRT)

partly due to its rich anatomical information and convenience of use. Target localization is one of the most important steps in IGRT procedures, and a primary reason for using CBCT is to determine the current position of the target and surrounding normal tissues inside the patient [1, 2, 3]. An accurate image of the target is essential for proper target positioning. Uncertainty of the target position requires the use of larger margins in treatment planning which can increase the likelihood of normal tissue complications. Therefore, an accurate image of the target reconstructed by CBCT can improve the chance of favorable patient outcome. The kV cone-beam imaging capability currently available with linear accelerator treatment systems provides excellent soft-tissue contrast and the potential for dose reduction compared to megavoltage (MV) CBCT images, an important benefit in IGRT.

However, total radiation dose to the patient from CBCT imaging prior to each fraction still poses a radiation safety concern [4]. Although the biological effects of imaging radiation dose on the tumor control probability of the target in IGRT require further investigation, it is desirable to spare imaging radiation dose to the normal tissues surrounding the target. Sparing dose to the normal tissues becomes imperative when these tissues are particularly radiation sensitive, such as eyes, breast or spinal cord. An accurate region-of-interest (ROI) imaging technique in this regard is a potentially important tool for routine CBCT in IGRT. ROI imaging here is used to mean that only the projection of a desired ROI is taken for each view, thereby reducing the dose outside of the ROI. Interestingly, in the report of AAPM Task Group 75, the authors envision that a more sophisticated reconstruction technique would be necessary to perform ROI imaging, and thereby reducing imaging radiation dose to the tissues outside the ROI [4]. In this paper we report the use of just such advanced reconstruction.

Some of the recently developed image reconstruction algorithms for CBCT can perform certain ROI reconstructions. [5, 6, 7, 8]. The chord-based backprojection-filtration (BPF) algorithm, for example, can produce accurate ROI images in general CBCT scanning configurations. Data truncation artifacts, often appearing in the reconstructed ROI images using conventional algorithms, can often be avoided by use of the chord-based BPF algorithm. However, for imaging targets located deep within the body the ROI becomes an interior problem, for which no stable, accurate image reconstruction method exists [9]. One approach using the local tomography method provides edge-enhanced images from ROI projection data [10], but this approach does not provide accurate image contrast information which is important in many applications including IGRT.

The proposed intensity-weighted region-of-interest (IWROI) imaging technique can reduce the imaging radiation dose to structures away from the imaging target,

while allowing solution of the reconstruction problem by using the chord-based BPF algorithm. We subdivide the reconstructed ROI into inner and outer regions, and illuminate the outer region with a filtered beam to decrease exposure during the scan. An intensity-weighting technique has been previously proposed for ROI imaging applications in diagnostics, but only with a conventional reconstruction algorithm which requires nontruncated data for accurate reconstruction [11, 12, 13]. A method using two scans, one of which is performed with a full field-of-view and low exposure and the other with a limited FOV and high exposure, has also been studied [14] but this method doubles the acquisition time. Our approach allows some types of data truncation without causing artifacts in the reconstructed ROI image and allows different exposure levels in two sub-ROIs from a single scan. In this work, we focus on circular CBCT, which is the dominant imaging modality employed in most radiation therapy systems, although the method can be extended to general scanning configurations such as the saddle trajectory.

2 Background

The Feldkamp-Davis-Kress (FDK) algorithm is the most widely used algorithm for 3-D circular CBCT image reconstruction because of its computational efficiency and acceptable image quality in many applications [15]. However, in the presence of transverse data truncation the FDK algorithm produces truncation artifacts in the reconstructed images. Since transverse data truncation is common if not unavoidable in ROI imaging, an algorithm that is more robust against transverse data truncation is desirable. The chord-based backprojection-filtration (BPF) algorithm is an analytic algorithm that can stably reconstruct ROI images on chords from truncated data. This capability of the BPF algorithm in ROI imaging has been exploited to potentially increase spatial resolution by using a larger geometric magnification in micro-CT applications [16].

2.1 Chord-based BPF algorithm for ROI imaging

The chord concept has been developed for exact image reconstruction of a CBCT with general source trajectories; it is rooted in the development of algorithms for helical CBCT. A chord is defined as a line segment connecting any two points on a continuous source trajectory. Specifically, in helical CBCT, a chord connecting two points on the trajectory within one turn is referred to as a PI-line segment. The chord-based BPF algorithm essentially decomposes the image into a number of chords that intersect the imaged object and collectively cover the ROI. The algorithm reconstructs the ROI image along the individual chords. In circular CBCT, since chords can be defined only

for the midplane in which the source trajectory resides, virtual source trajectories have been introduced for off-midplanes. Additionally, we have introduced virtual chords that connect any two points on the virtual source trajectories. Approximate image reconstruction, therefore, can be performed by use of the BPF algorithm for those off-midplanes [17, 18]. Derivatives of the cone-beam data acquired by a circular scan are backprojected first onto each chord, followed by the filtering along each chord in one-dimension. In the FDK algorithm the filtering occurs in the projection data, thus transverse truncation can produce artifacts in the reconstructed images . In contrast, as long as the imaged object is not truncated along a given chord, the image on the chord can be reconstructed accurately by the chord-based BPF algorithm despite truncations in the projection data. This is the key feature of the chord-based BPF algorithm that enables accurate ROI imaging.

2.2 IWROI image reconstruction in circular CBCT

In many IGRT applications such as prostate cancer treatment, the imaging target is located deep within the tissue. In this case, we can subdivide the ROI into two regions: inner ROI and outer ROI. The inner ROI can be selected to cover the imaging target, for example the prostate and nearby organs at risk. The outer ROI would be the remainder of the imaged volume and would include some of the skeletal structures which can be used for image registration. A higher noise level may be tolerable in the outer ROI for skeletal registration as compared to the inner ROI where maximum image quality is required for soft tissue discrimination. Therefore, we propose to scan the patient with two different levels of exposure: full exposure to the inner ROI and reduced exposure to the outer. This can be simply implemented using suitable filters in the x-ray beam. Reduced exposure in the outer ROI will decrease the patient dose due to imaging. Additionally the decreased fluence will result in less scatter from the patient's body. Accordingly, the quantum noise level in each projection will be higher in the outer region. Noise properties of the chord-based BPF algorithm have been carefully investigated and it has been shown that the noise of the reconstructed image along a chord is localized in a practical sense [19, 20]. This means that the higher noise level in the outer ROI will not substantially affect the noise level in the inner ROI after reconstruction. Figure 1 schematically illustrates the noise propagation in the image reconstruction. Different noise levels in the projection data are merged onto a chord support-segment after backprojection, and noise levels remain well separated even after filtration. Numerical simulation studies have successfully verified this noise confinement property of the algorithm in IWROI imaging [21]. The convolution kernel

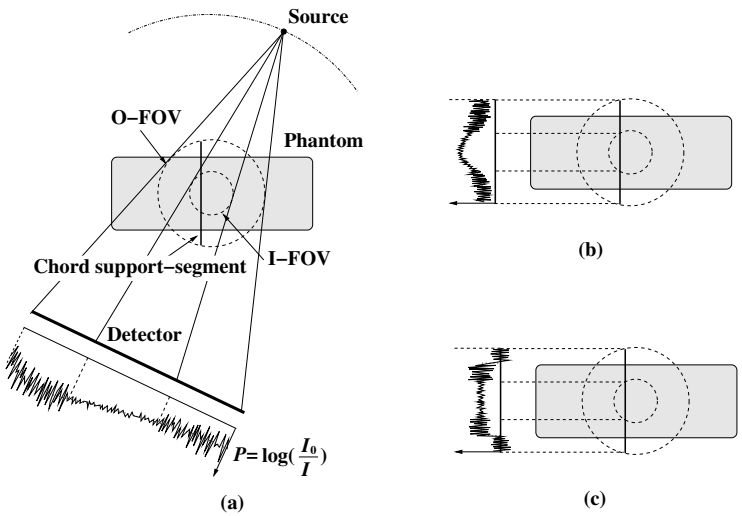

Figure 1: (a) For each view, the projection data can be separated into two regions having less noise due to higher exposure and vice versa. The noise levels are almost locally confined after (b) backprojecting the data on to a chord support-segment, and (c) filtration along the chord. Cone-beam data P is calculated from I_0 and I, which stand for flood-field (referred to as open-field in this paper) and projection, respectively.

used in the FDK algorithm is also relatively localized, so that the intensity-weighted imaging technique can be utilized with the FDK algorithm in cases where data truncation is negligible or can be compensated for. However, as will be demonstrated, even advanced correction schemes applied in conjunction with FDK cannot correct for large truncations, which may occur for ROI imaging of some anatomical sites.

3 Methods

3.1 System and filters

The imaging work presented here was done with the on-board imaging (OBI) system on a Trilogy linear accelerator (Varian Medical Systems). The OBI system is composed of an x-ray source and flat panel detector mounted on the accelerator gantry orthogonal to the treatment beam as shown in Fig. 2. The scanning parameters used in this work are summarized in Table 1. A standard clinical scanning protocol with

Source		Detector		Geometry	
Parameter	*Value*	*Parameter*	*Value*	*Parameter*	*Value*
Mode	Full-fan	Size_x	39.73 cm	SAD	100 cm
kVp	125 kV	Size_y	29.80 cm	SDD	149.9 cm
mA	80 mA	Pixel pitch	194 μm	Start angle	-182°
ms	13 ms	Pixel matrix	2048×1536	Stop angle	178°
Collimator_x	±13.5 cm	Binning	2×2	# projections	~ 860
Collimator_y	±3.0 cm	Eff. pixels	1024×768		

Table 1: System parameters.

bowtie filter in place utilized beam current 80 mA and a 25 ms pulse. This study removed the bowtie filter leaving portions of the beam completely unfiltered, thus the exposure time was reduced to 13 ms to achieve reasonable intensity levels for open-field images. For reconstruction consistency, acquisition was always performed using a counter-clockwise gantry rotation. The field was narrowly collimated in the axial (y) direction to minimize scatter effects in the reconstructed image. It was found that even with such a narrow field, scatter is great enough that a scatter correction is required. Four sets of filters were used for the intensity weighting, two each of copper and aluminum. For brevity the filters will be referred to with the following naming convention; Cu1, Cu2, Al1, and Al3 representing 0.32 cm, 0.64 cm, 1.60 cm, and 4.80 cm thicknesses respectively. These thicknesses were chosen to provide great enough separation of intensity levels in the filtered regions, in order to quantify the corresponding changes in image noise. The filters were simple rectangular slabs with square edges, and attached to a spare bowtie filter mounting plate.

3.2 Phantoms

Three different phantoms were used for this study. The first was a solid-water (SW) phantom which consisted of 30×30 cm solid-water slabs, commonly available in radiation oncology clinics, stacked 16 cm high. A separate phantom was used for contrast to noise ratio (CNR) measurements, which we refer to as the CNR-phantom. This phantom was similarly made from a stack of solid water slabs with a sheet of lucite as a low contrast element and two Teflon rods as high contrast elements. Finally a pelvis phantom was also imaged, consisting of a partial skeleton ranging from the L1 lumbar vertebra through the mid femur, embedded in lucite formed into a human shaped contour. There were however no soft tissue inhomogeneities in this phantom.

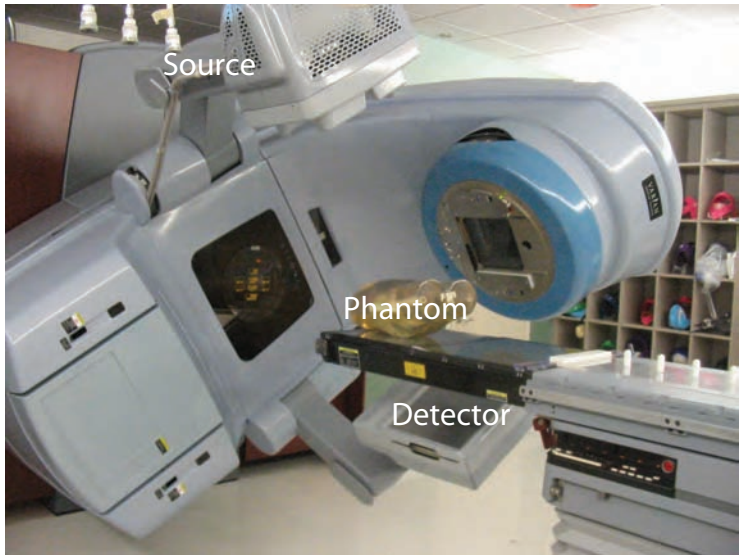

(a)

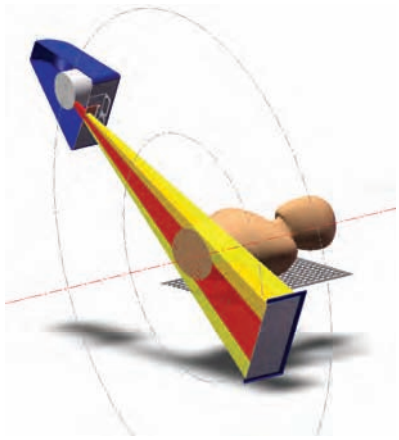

(b)

(c)

Figure 2: The OBI system used in the experiment. (a) A picture of the system. (b) Schematic view of the imaging configuration. (c) A picture of the kV source with the IW-filters mounted.

3.3 Data corrections

Although the use of IW-filters can help decrease scatter in cone-beam projections, the presence of scatter can still be a limitation to image quality and accuracy. Additionally, local variations in beam-quality due to hardening by the IW-filters can substantially alter the image accuracy; a harder beam lowers the estimated attenuation coefficient. Both of these physical factors, if uncorrected, can degrade image quality. We used a simple, direct method proposed by Siewerdsen *et al*. for scatter estimation [22]. A first-order approximate correction method for the beam-quality effect was used. Note that we use the term "beam-quality effect" rather than "beam hardening" to emphasize that this is not a beam hardening correction as usually understood, which deals with hardening of the beam as it penetrates the patient.

3.3.1 Scatter correction

The scatter estimation method [22] for cone-beam projections is based on the assumption that the detector signal measured in regions behind the collimator blades is attributable to x-ray scatter. Because the algorithm estimates scatter fluence directly from the projection data, it is robust to a number of variations that exist in cone-beam scans including imaging configuration, patient motion, system geometry and so on. For each projection we used a second-order polynomial interpolation from the collimator shadows to estimate column-wise scatter fluence. An estimate of the 2D scatter fluence was then obtained by lateral smoothing of the column-wise scatter estimates across all columns. The estimated 2D scatter fluence was subtracted from original projection resulting in an estimate of the primary image. Each of the steps in the correction method are illustrated in Fig. 3.

3.3.2 Heterogeneous beam-quality correction

The reconstruction process involves transformations of the cone-beam data (represented as P in Fig. 1) rather than the raw projection data. The cone-beam data ideally represents the integrated attenuation along each ray. For the present study, this was calculated as the natural logarithm of the ratio of the open field intensity map to the acquired projection. The open field intensity was measured by taking a repeat scan with the same x-ray technique, geometric parameters and filters in place, but the couch and phantom removed from the field of view. The division process in calculating P should normalize out the reduced beam intensity of the filtered region. However, since this beam has been hardened by the filter, the computed attenuation values will be lower than in the unfiltered region. In order to increase the accuracy of the image values in

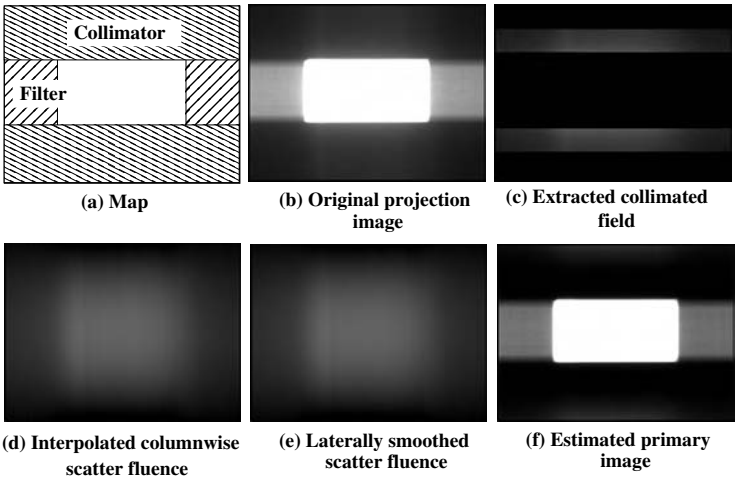

Figure 3: Scatter correction procedure is illustrated with example images. (a) The collimators and the IW-filters are positioned. (b) Original projection image of a phantom. (c) Projection data under the collimators are extracted. (d) Column-wise interpolation is applied for each column. (e) Lateral smoothing is performed to finally estimate the scatter fluence. (f) Original image subtracted by the estimated scatter fluence.

the filtered region and increase value consistency with the unfiltered region, a simple first order approximate correction scheme was applied. The assumption was made that the energy spectra of the beams could be represented by single average energies. Additionally, the assumption was made that the ratio of linear attenuation coefficients for the two energies was similar to that of water, for all imaged materials. The second assumption is expected to be valid for air, water, and muscle in the x-ray energy range used in this work, but to slightly underestimate the ratio for bone. Following this assumption, the beam quality correction was performed by simply multiplying the cone-beam data P under the IW-filter by the estimated ratio of attenuation coefficients without and with the filter. This was estimated from the anterior-posterior (AP) projection of the solid water phantom, where there was an almost uniform thickness of uniform material for both filtered and unfiltered rays . Variation of the thickness due to obliquity was computed to have less than 0.2% effect on the reconstructed image. The square edges of the IW-filters resulted in a geometric penumbra region in the projection image, and interpolated ratio values were used in this transition region.

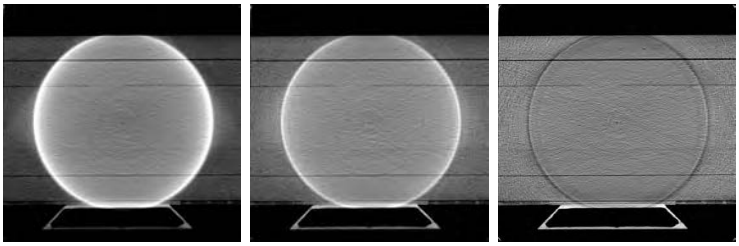

(a) (b) (c)

Figure 4: Transverse slice images of the reconstructed SW-phantom scanned with Cu1-filter are displayed; (a) No correction, (b) scatter correction, and (c) scatter + beam quality correction have been applied. Display window is [0.1, 0.3] cm^{-1}. Inner and outer ROIs can be easily distinguished by the pronounced ring artifact in this figure and in all the following figures.

4 Results

4.1 Data corrections

All of the results presented in the following sections are based on corrected data, where the scatter correction and the beam-quality correction have both been applied to the projection data. Unless otherwise noted the boundary between the inner and outer regions can be visualized in the images as the prominent ring due to the sharp transition in intensity which has not yet been corrected for. All images presented here represent the full reconstructed region and have not been cropped in any direction, so an object reaching the lateral extent of the image signifies transverse truncation.

Examples of uncorrected and partially corrected data are shown to visualize the effects of data corrections in this section. In Fig. 4 we display reconstructed images of the SW-phantom scanned with the Cu1-filter (a) before any correction, (b) after scatter correction, and (c) after scatter and beam quality correction. A cupping artifact due to scatter is observed in Fig. 4(a), and is suppressed substantially (b). Image uniformity is recovered after beam quality correction (c). The same correction parameters have been applied in the pelvis phantom scan to see the correction effects for a more realistic case, and the results are displayed in Fig. 5.

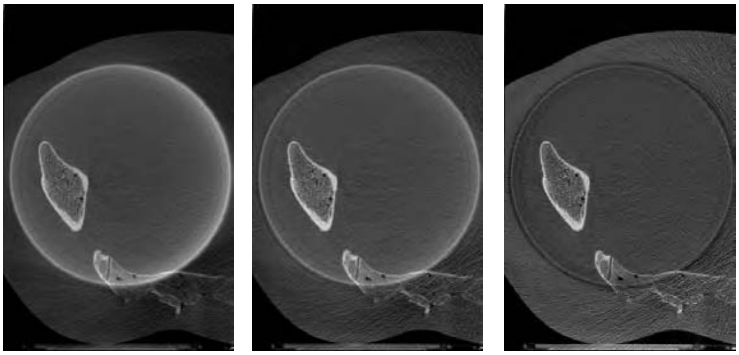

(a) **(b)** **(c)**

Figure 5: Transverse slice images of the reconstructed pelvis phantom scanned with Cu1-filter are displayed; (a) No correction, (b) scatter correction, and (c) scatter + beam quality correction have been applied. Display window is [0.1, 0.6] cm^{-1}.

	Inner (%)	Outer (%)
Cu1	0.05	0.14
Cu2	0.05	0.4
Al1	0.05	0.07
Al3	0.06	0.2

Table 2: Noise levels (coefficients of variation) measured in inner and outer ROIs of the SW-phantom.

4.2 Noise study

A noise evaluation study was performed with the SW-phantom for each of the four different filters. Small square regions were selected from each image within the inner and outer ROIs for statistical analysis. Coefficients of variation (standard deviation divided by the mean value) were computed and the results are summarized in Table 2.

4.3 CNR study

Similarly, a CNR evaluation study was performed with the CNR phantom for each of the four filters. Eight small rectangular regions were selected from each image, four

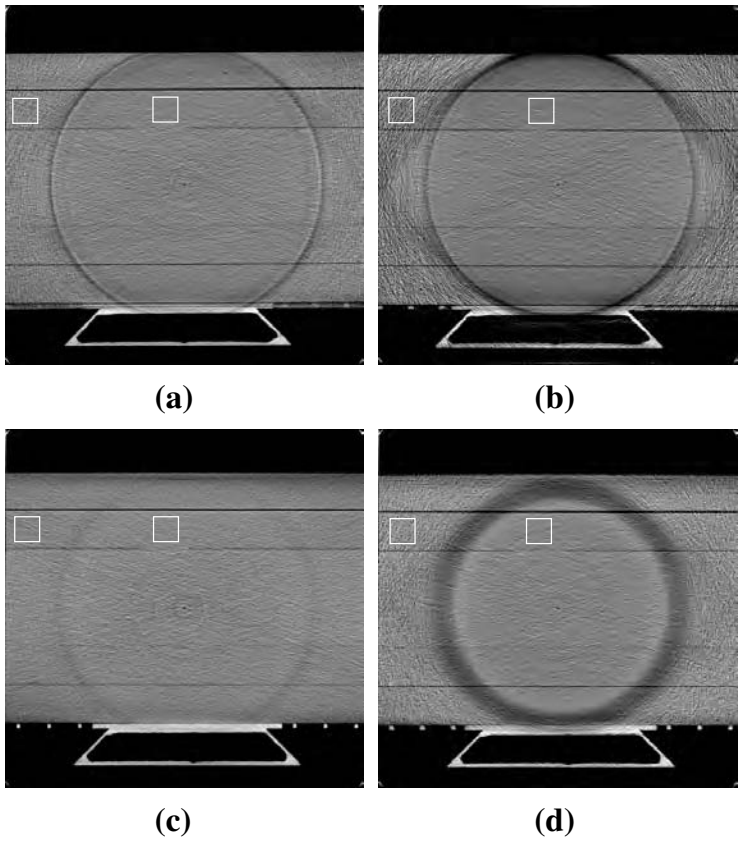

Figure 6: Transverse slice images of the reconstructed SW-phantom scanned with (a) Cu1-filter, (b) Cu2-filter, (c) Al1-filter, and (d) Al3-filter. Display window is [0.1, 0.3] cm^{-1}.

	Teflon						Lucite					
	Inner			*Outer*			*Inner*			*Outer*		
	Contr.	Noise	CNR	Contr.	Noise	CNR	Contr.	Noise	CNR	Contr.	Noise	CNR
Cu2	0.152	1.75E-4	869	0.121	1.15E-3	105	1.21E-2	2.37E-4	51.0	6.08E-3	9.55E-4	6.40
Cu1	0.146	1.91E-4	764	0.155	3.67E-4	422	1.10E-2	2.49E-4	44.2	1.21E-2	3.47E-4	34.9
Al3	0.144	2.48E-4	581	0.139	8.28E-4	168	8.57E-3	2.22E-4	38.7	5.89E-3	7.60E-4	7.80
Al1	0.132	2.58E-4	512	0.159	2.50E-4	636	1.04E-2	2.83E-4	36.9	1.25E-2	2.58E-4	48.2

Table 3: CNR measured for high contrast medium (Teflon) and for low contrast medium (Lucite) with respect to solid water in inner and outer ROIs. Contrast and noise are in units of cm^{-1}.

each in the inner and outer regions, positioned within the contrast media and nearby solid water background. The upper pairs in the images in Fig. 7 were used for the calculation of the contrast to noise in Teflon and the lower set for lucite. For a given contrast material (medium1), e.g. Teflon rod, the adjacent solid-water region (medium2) was selected for the CNR calculation. CNR in this study was defined as in Eq. 1

$$\mathrm{CNR} = \frac{\mathrm{Mean1} - \mathrm{Mean2}}{(\mathrm{StandDev1} + \mathrm{StandDev2})/2}, \tag{1}$$

where Mean1 & 2 stand for the mean values of medium1 & 2, and StandDev1 & 2 represent the standard deviations of medium1 & 2, respectively. The results are summarized in Table 3.

4.4 Pelvis phantom

To test the method in a quasi-clinical setting, we used the pelvis phantom. Although it does not have any soft-tissue regions, it contains bony structures that can be assessed qualitatively or quantitatively for further studies such as image registration. Reconstructed images along transverse, coronal and sagittal planes are shown in Fig. 8 for four IW-filters.

5 Discussion

There have been a number of reported efforts to reduce imaging radiation dose outside an ROI by use of filters. Zonal filters have been used to reduce exposure outside of the windowed region along the longitudinal direction, which does not achieve ROI

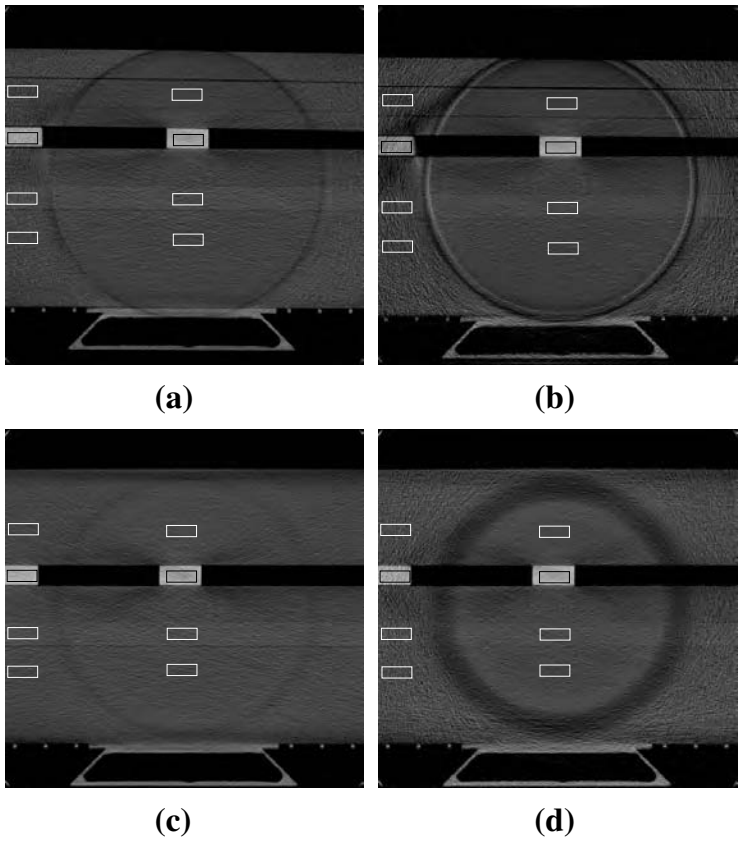

Figure 7: Transverse slice images of the reconstructed CNR-phantom scanned with (a) Cu1-filter, (b) Cu2-filter, (c) Al1-filter, and (d) Al3-filter. Display window is [0.1, 0.6] cm^{-1}.

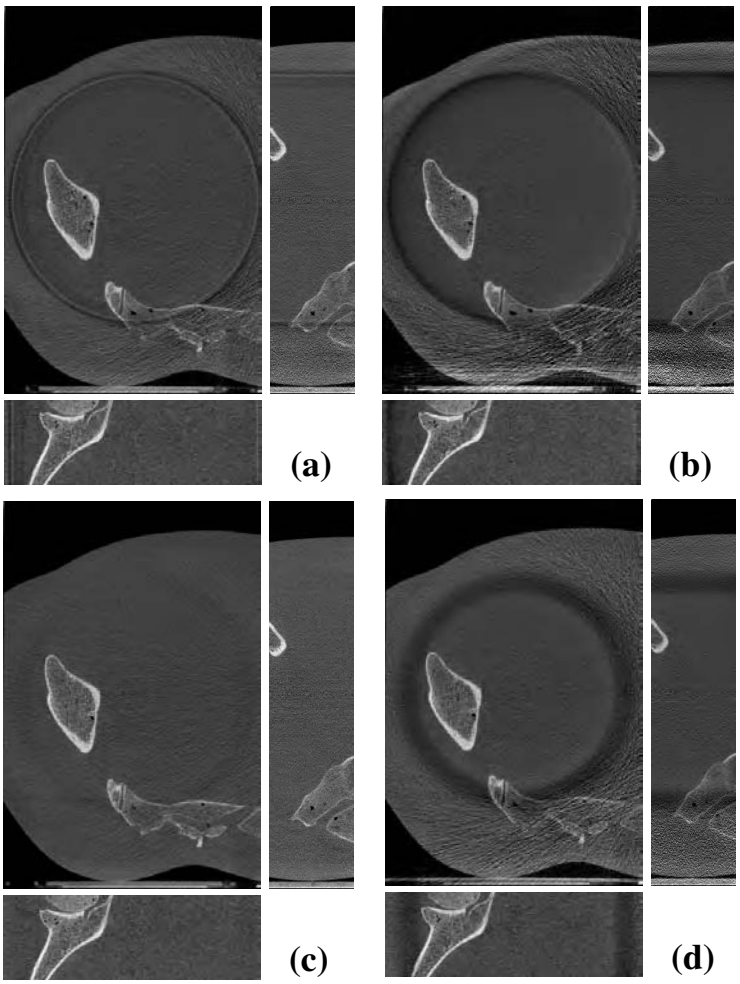

Figure 8: Slice images - transverse (center), sagittal (right), and coronal (bottom) images - of the reconstructed pelvis phantom scanned with (a) Cu1-filter, (b) Cu2-filter, (c) Al1-filter, and (d) Al3-filter. Display window is [0.1, 0.6] cm^{-1}.

imaging in transverse planes [23]. ROI filters have also been used for diagnostic purposes such as angiography, head scan, and breast scan [11, 12, 13]. However, since only conventional reconstruction based on the FDK algorithm has been employed, transverse data truncation can cause problems in these methods. An example of truncation artifacts is shown in Fig. 9 (b), where the same amount of projection data used in our work was used for image reconstruction by the FDK algorithm. There exist approximate methods such as data extrapolation for reducing data truncation artifacts, and they may improve the image quality substantially depending on the degree of data truncation in an imaging task. However, because the proposed IWROI imaging technique often involves considerable data truncation, a simple correction scheme such as symmetric mirroring extrapolation [24] may not work as well as in more favorable applications. For example, if a breast is selected as the ROI in breast IGRT, the entire body outside of the breast region will be truncated. As shown in Fig. 9 (c), a linear extrapolation leads to over-correction in the pelvis example, because the data near one edge of the detector tends to decrease slowly or even increase in some projection angles. Because the convolution kernel in the FDK algorithm has a long negative tail, the extrapolated data in this case contribute to lowering the pixel values after filtering and backprojection. Although it may be possible to devise an approximate correction scheme more appropriate than a simple extrapolation in certain situations, assumptions of accuracy and robustness against serious data truncation that may arise in a variety of ROI imaging tasks are generally unwarranted. The chord-based BPF algorithm in contrast achieves accurate image reconstruction in the face of a large degree of data truncation, which is a fundamental and often important advantage, for example when CT numbers are to be used as input to radiation transport calculations, or intensity-based segmentation or registration methods. Of course, there may also be situations in which the inaccuracies in FDK reconstructions from truncated data can be acceptable.

The proposed IWROI technique can achieve far more dose reduction than conventional approaches [11, 12, 13] without appreciably sacrificing ROI image quality, because the robustness to transverse data truncation allows the illuminated region to be further reduced. The zonal filter approach [23] is not directly comparable with the IWROI technique in terms of dose saving because it cannot deal with ROI imaging tasks with transverse data truncations, although it can be considered a synergistic way to improve dose management. A variety of clinical scanning tasks can be performed by use of the IWROI technique, including a breast scan, hemi-thorax lung scan, and central-pelvis scan among many others.

IW-filters are fundamentally different from bow-tie filters, which are widely used

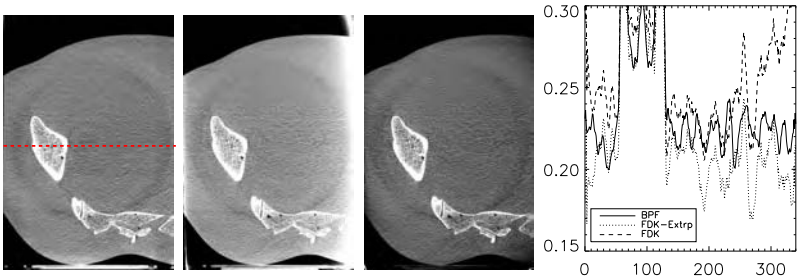

Figure 9: Truncation artifacts are pronounced in (b) where the FDK algorithm has been used for image reconstruction with the same amount of data that were used in (a) by the chord-based BPF algorithm. The corresponding image reconstructed by the FDK algorithm with a linear extrapolation correction is shown in (c). Display window of [0.14,0.32] cm^{-1} is used for all images to enhance visualization of the artifacts. Line profiles of the three images along the dashed line shown in (a) are plotted in (d). Solid line represents (a), dotted line (b), and dashed line (c). For better visualization, eight-point smoothing has been used to generate line profiles.

in clinical systems such as OBI, in that the primary purpose of the bow-tie filter is to improve overall image quality [25]. Attenuation of the beam particularly at the peripheral regions of the patient allows the signal intensity to stay within the dynamic range of the detector. Reduced scatter due to attenuation of the beam can also contribute to better image quality. Imaging radiation dose reduction to the patient is an additional advantage of using bow-tie filter, although it is not the primary concern. IW-filters are introduced to reduce imaging-radiation dose to the patient substantially by sacrificing the image quality in selected regions. Therefore the amount of beam filtration from the IW-filters is substantially greater than that of the bow-tie filters. In order to estimate the amount of beam filtration, exposure was measured with each filter using a Keithley parallel plate ion chamber (75972) and dosimeter (35050A). The results are summarized in Table 4. Although some reduction of exposure has been achieved by the Al1-filter which is close to a conventional bow-tie filter in thickness, the ratio of the reduction becomes much greater when other filters are used. Scatter fraction was estimated by use of Siewerdsen's method for AP projection images of the SW-phantom for each filter. Scatter fraction values from the central region are listed in Table 4 as well. It is interesting to note that the results support the fact that the use of bow-tie filter, i.e. the IW-filters in this case, contributes to scatter reduction, although it can be difficult to quantitatively relate the reduction of scatter to the reduction of exposure

	Exposure (mR)	Scatter Fraction (%)
No filter	77.6	10.1
Al1	14.1	9.4
Al3	1.74	7.7
Cu1	2.81	8.4
Cu2	0.62	8.0

Table 4: Exposure was measured 10 times at 125 kVp, 80 mA, 65 ms for each case, and average values are listed. Scatter fraction is estimated in the middle of AP projections of the SW-phantom.

partly due to relatively rough estimation method of scatter.

Throughout the reconstructed images in the previous section, ring artifacts are pronounced although the severity varies depending on filter type and thickness. We would like to draw a distinction between the ring artifacts here and the ring artifacts conventionally encountered. Conventional ring artifacts result primarily from nonuniform detector response, which is generally well corrected for in this data. The ring artifacts in this work can be attributed to several factors: inaccurate correction of scatter and heterogeneous beam-quality, filter shape and position, and gravitationally induced pointing errors in the x-ray source. Since our correction methods are approximate and only first-order, they may in fact amplify data inconsistency resulting in the ring artifacts. Asymmetry of the filter positions in terms of rotation axis would result in a ring-band structure in the images. The aforementioned deficiencies in correction methods and filter position asymmetry are thought to be the primary causes of the thick drop-out in the images with Al3-filter. The sharp edges of the filters may also aggravate the effects of the asymmetry and thus increase inconsistency between projection data. Pointing errors and vibration in the source can cause inconsistencies in the transition region that may also increase these artifacts. Accounting for edge effects in the filter design may help minimize the ring artifacts. Pre- or post-reconstruction correction algorithms for ring artifacts can be utilized as well, if necessary [26].

Noise properties of the reconstructed images depend on a number of factors including exposure, electronic noise, energy response of the detector, and reconstruction algorithm. Although more rigorous analysis based on models such as cascaded linear systems of the overall imaging system can help to better understand the image noise, exposure plays a dominant role in determining the noise level of reconstructed images because the imaging system is quantum limited, for scanning parameters used in this work [27]. Slightly higher noise in the inner ROI with Al3-filter compared to others

is thought to be due to more contamination of the data by scatter from this thick filter. CNR is also related to the factors that affect noise and in addition, it is susceptible to additional image artifacts such as metal artifacts. Teflon rods create streak patterns around them, and degrade image uniformity not only of the rods themselves but also of the neighboring materials. However, inner ROI CNRs of the high contrast material (Teflon) and the low contrast material (Lucite) in solid water are both up to about eight times higher than outer ROI CNRs. Image artifacts are thought to dominate CNR characteristics in Al1-filter case, where an inversion of the expected values was observed.

Measurement of the dose reduction by use of the IW-filters is in progress and will be reported elsewhere. The influence of image CNR on accuracy of image registration in IGRT must also be investigated so that the proper design of the IW-filter can be obtained, for both dose reduction and successful image guidance. Although only a full-fan geometry, where the rotation axis is projected onto the central vertical line of the detector, is assumed in this work, a half-fan geometry in which the rotation axis is projected onto an off-central vertical line of the detector can also be used for the proposed IWROI imaging. The extended FOV of a half-fan geometry can be particularly useful for obese patients.

6 Summary

Imaging radiation dose to a patient by repeated CBCT poses a patient radiation safety concern. In this regard, ROI imaging which limits dose mostly to the imaging target is desirable. Since ROI imaging of the target in many cases leads to an interior problem, we devised the IWROI method, which illuminates an outer ROI around the target with a reduced fluence, thereby permitting accurate reconstruction. Accurate image information within the inner ROI is maintained as required for tumor localization, whereas relatively poorer image quality in the outer ROI can still result in acceptable image registration in IGRT. The proposed method can reconstruct the target image with high CNR and the surrounding tissue image with relatively low CNR. Data truncation artifacts can be avoided by using the proposed chord-based BPF-type algorithm, and noise propagation from outer ROI to inner ROI is well-suppressed due to the noise properties of this algorithm. We believe the proposed approach is a promising new technique for CBCT in IGRT.

Acknowledgments

The authors would like to thank K. Farrey for his help on using the OBI system and Dr. G. Ding at Vanderbilt University for his granting our use of the spectrum data of the OBI system. S. Cho is supported in part by a DOD predoctoral training grant PC061210. E. Pearson is supported by NIH predoctoral training grant T32 EB002103. This work was supported in part by Varian Medical Systems, Palo Alto, CA, and in part by National Institutes of Health grants EB00225 and CA120540. Partial funding for this work was also provided by the NIH S10 RR021039 and P30 CA14599. The contents of this paper are solely the responsibility of the authors and do not necessarily represent the official views of any of the supporting organizations.

References

[1] D. A. Jaffray, "Emergent technologies for 3-dimensional image-guided radiation delivery," *Semin. Radiat. Oncol.*, vol. 15, pp. 208–216, 2005.

[2] L. Xing, B. Thorndyke, E. Schreibmann, Y. Yang, T.-F. Li, G.-Y. Kim, G. Luxton, and A. Koong, "Overview of image-guided radiation therapy," *Medical Dosimetry*, vol. 31, pp. 91–112, 2006.

[3] J. M. Balter and M. L. Kessler, "Imaging and alignment for image-guided radiation therapy," *J. Clin. Oncol.*, vol. 25, pp. 931–937, 2007.

[4] M. J. Murphy, J. Balter, S. Balter, J. A. Bencomo, I. J. Das, S. B. Jiang, C. M. Ma, G. H. Olivera, R. F. Rodebaugh, K. Ruchala, H. Shirato, and F. F. Yin, "The management of imaging dose during image-guided radiotherapy: Report of the AAPM Task Group 75," *Med. Phys.*, vol. 34, pp. 4041–4063, 2007.

[5] Y. Zou and X. Pan, "Image reconstruction on PI-lines by use of filtered backprojection in helical cone-beam CT," *Phys. Med. Biol.*, vol. 49, pp. 2717–2731, 2004.

[6] Y. Zou, X. Pan, and E. Y. Sidky, "Theory and algorithms for image reconstruction on chords and within regions of interest," *Journal of the Optical Society of America*, vol. 22, pp. 2372–2384, 2005.

[7] F. Noo, R. Clackdoyle, and J. Pack, "A two-step Hilbert transform method for 2D image reconstruction," *Phys. Med. Biol.*, vol. 49, pp. 3903–3923, 2004.

[8] J. D. Pack and F. Noo, "Cone-beam reconstruction using 1D filtering along the projection of M-lines," *Inv. Prob.*, vol. 21, pp. 1105–1120, 2005.

[9] F. Natterer, *The Mathematics of Computerized Tomography*. New York: J. Wiley & Sons, 1986.

[10] A. Faridani, D. V. Finch, E. L. Ritman, and K. T. Smith, "Local tomography II," *SIAM J. Appl. Math.*, vol. 57, pp. 1095–1127, 1997.

[11] R. Chityala, K. R. Hoffmann, D. R. Bednarek, and S. Rudin, "Region of interest (ROI) Computed Tomography," *Proc. SPIE*, vol. 5368, pp. 534–541, 2004.

[12] R. Chityala, K. R. Hoffmann, S. Rudin, and D. R. Bednarek, "Region of interest (ROI) computed tomography (CT): Comparison with full field of view (FFOV) and truncated CT for a human head phantom," *Proc. SPIE*, vol. 5745, pp. 583–590, 2005.

[13] L. Chen, C. C. Shaw, M. C. Altunbas, C.-J. Lai, X. Liu, T. Han, and T. Wang, "Feasibility of volume-of-interest (VOI) scanning technique in cone beam breast CT - a preliminary study," *Med. Phys.*, vol. 35, pp. 3482–3490, 2008.

[14] D. Letourneau, J. W. Wong, M. Oldham, M. Gulam, L. Watt, D. A. Jaffray, J. H. Siewerdsen, and A. A. Martinez, "Cone-beam CT guided radiation therapy: technical implementation," *Radiotherapy and Oncology*, vol. 75, pp. 279–286, 2005.

[15] L. A. Feldkamp, L. C. Davis, and J. W. Kress, "Practical cone-beam algorithm," *J. Opt. Soc. Am.*, vol. A1, pp. 612–619, 1984.

[16] S. Cho, J. Bian, C. A. Pelizzari, C. T. Chen, T. C. He, and X. Pan, "Region-of-interest image reconstruction in circular cone-beam microCT," *Med. Phys.*, vol. 34, pp. 4923–4933, 2007.

[17] X. Pan, D. Xia, Y. Zou, and L. Yu, "A unified analysis of FBP-based algorithms in helical cone-beam and circular cone- and fan-beam scans," *Phys. Med. Biol.*, vol. 49, pp. 4349–4369, 2004.

[18] L. Yu, Y. Zou, E. Y. Sidky, and X. Pan, "Region of interest reconstruction from truncated data in circular cone-beam CT," *IEEE Trans. Med. Imag.*, vol. 25, pp. 869–881, 2006.

[19] D. Xia, L. Yu, E. Sidky, Y. Zou, N. Zuo, and X. Pan, "Noise properties of chord-image reconstruction," *IEEE Trans. Med. Imag.*, vol. 26, pp. 1328–1344, 2007.

[20] X. Han, D. Xia, E. Y. Sidky, and X. Pan, "Investigation of the noise properties of the Hilbert transforms," *IEEE Trans. Med. Imag.*, to be submitted.

[21] S. Cho, E. Pearson, D. Xia, X. Han, C. Pelizzari, and X. Pan, "A preliminary study of intensity-weighted ROI imaging in cone-beam CT," in *Proc. SPIE*, vol. 6913, p. 69132C, 2008.

[22] J. H. Siewerdsen, M. J. Daly, B. Bakhtiar, D. J. Moseley, S. Richard, H. Keller, and D. A. Jaffray, "A simple, direct method for x-ray scatter estimation and correction in digital radiography and cone-beam CT," *Med. Phys.*, vol. 33, pp. 187–197, 2006.

[23] C. J. Moore, T. E. Marchant, and A. M. Amer, "Cone beam CT with zonal filters for simultaneous dose reduction, improved target contrast and automated set-up in radiotherapy," *Phys. Med. Biol.*, vol. 51, pp. 2191–2204, 2006.

[24] B. Ohnesorge, T. Flohr, K. Schwarz, J. P. Heiken, and K. T. Bae, "Efficient correction for ct image artifacts caused by objects extending outside the scan field of view," *Med. Phys.*, vol. 27, pp. 39–46, 2000.

[25] S. Yoo and F. Yin, "Dosimetric feasibility of cone-beam CT-based treatment planning compared to CT-based treatment planning," *Int. J. Radiat. Oncol. Biol. Phys.*, vol. 66, pp. 1553–1561, 2006.

[26] J. Sijbers and A. Postnov, "Reduction of ring artefacts in high resolution micro-CT reconstructions," *Phys. Med. Biol.*, vol. 49, pp. N247–N253, 2004.

[27] G. X. Ding, M. Duggan, and C. W. Coffrey, "Characteristics of kilovoltage x-ray beams used for cone-beam computed tomography in radiation therapy," *Phys. Med. Biol.*, vol. 52, pp. 1595–1615, 2007.

Prior-image-based few-view cone-beam CT for applications to daily scan in image-guided radiation therapy: Preliminary study

[1,2]Seungryong Cho, [2]Erik Pearson, [1]Emil Y. Sidky, [1]Junguo Bian, [2]Charles A. Pelizzari, and [1]Xiaochuan Pan
[1]Department of Radiology, University of Chicago, Chicago, IL 60637
[2]Department of Radiation and Cellular Oncology, University of Chicago, Chicago, IL 60637

Abstract

Interfraction motion of a treatment target such as the prostate in radiation therapy (RT) is, in part, responsible for large planning target volume (PTV) margins and related side effects. Online adjustment of the treatment based on timely cone-beam CT (CBCT) images can be particularly useful for patients with large interfraction motion. However, radiation dose to the patient due to frequent CBCT poses a radiation safety concern. One unique feature of CBCT for interfraction motion detection is the availability of a prior anatomical image most of which has not changed. We propose an iterative algorithm, for image reconstruction from a very limited number of projections in CBCT, that is based on total variation (TV) minimization subject to the constraints of data fidelity and positivity and that utilizes anatomical image prior information. Numerical studies for a 2D fan-beam geometry suggests the proposed algorithm can potentially contribute to lowering the radiation dose to the patient by allowing satisfactory image reconstruction from a very limited number of projections.

1 Introduction

Online adaptive radiotherapy based on in-room kV CBCT system allows for soft-tissue registration, which is one-step correction process taking into account patient setup error and internal organ motion at the same time [1, 2]. Reduced treatment margins as a result of online adjustment can be particularly useful for patients with large random interfraction motion. Therefore, daily CBCT for target localization in image-guided radiation therapy (IGRT) is becoming a clinical choice for many sites including the prostate. However, radiation dose delivered to the patient due to frequent CBCT may pose a challenge in the patient's radiation safety [3]. Few-view CBCT is one approach to reduce imaging-radiation dose and has thus recently drawn investigator's attention. Image reconstruction algorithms have been actively developed for few-view CBCT. One unique feature of CBCT for interfraction motion detection is the availability of prior anatomical images which are substantially unchanged. A prior image may be available from the previous fraction CBCT scan, or an initial CBCT set-up scan.These scans contain the same anatomical information as the current scan except for anatomical changes due to internal motion or patient weight gain/loss. However, a substantial portion of the image, particularly including bony structures and surrounding tissues, remains unchanged. We propose an iterative algorithm in this paper for image reconstruction from a very limited number of projections in CBCT, which is based on minimization of the image TV subject to the constraints of data fidelity and positivity and that utilizes information available from a prior image.

Traditional iterative approaches for image reconstruction have been of an unconstrained minimization type where the object function to be minimized combines data fidelity and regularization terms. Such an approach can provide a unique (or very limited set of) solution(s) that minimizes the object function when the projection data are complete or fully sampled in a practical sense. However, when the projection data are incomplete (e.g. few-view data), the

problem becomes more under-determined and there will, in general, be many solutions consistent with the projection data. Regularization terms are supposed to select the optimum solution among them in this case, and therefore it is natural to regard the problem as a constrained optimization one where the regularization term is the objective function and data fidelity is a constraint. Image TV, which is ℓ_1-norm of the image gradient, has been widely used as a regularization term, particularly for edge-preservation, and TV-based constrained optimization approach (a.k.a. compressed sensing image reconstruction) has recently been introduced to CBCT [4, 5].

Incorporation of prior knowledge has been investigated in iterative image reconstruction approaches to improve the image accuracy and quality. Several approaches have been considered specifically for cases when a prior image is available. A minimum-weighted norm reconstruction using the reciprocals of the values of the prior image as the weight vectors has been developed to reconstruct signals from incomplete data [6]. Using the image reconstructed from the complete data, although contaminated by periodic motion of the anatomy, by an analytic algorithm as prior image, a compressed sensing type CT reconstruction for a limited number of projections at the same phase has been proposed [7]; the algorithm uses a weighted sum of image TV and difference image (current image - prior image) TV as the objective function to minimize. However, optimization of the weighting factors in addition to the iteration parameters has to be performed. Feasibility of using anatomical CT/MRI images for image reconstruction in PET/SPECT to improve image quality has been investigated [8]. Investigators have also showed that the amount of samples needed from a signal with sparse discrete-time Fourier transform can be reduced compared to the original compressed sensing approach if information on the support of the sparse domain can be employed [9]. This approach of utilizing the prior information is essentially very close to the proposed algorithm in this paper.

That a prior image is readily available in IGRT applications provides a new opportunity for iterative algorithms; direct use of the prior image itself merits thorough investigation. We have previously proposed a TV algorithm utilizing prior image with internal motion as an initial guess in few-view fan-beam CT, and successfully demonstrated that the number of views for image reconstruction can be reduced from that needed in the TV algorithm without prior in the numerical study (roughly speaking, from 20 views to 10 views) [10]. Using the prior image as an initial image estimate in the iterative process is thought to help find the true minimum TV image that meets the data fidelity constraint, whereas a local minimum may be found when no prior image information is used. However, it was observed that the unchanged portion of the prior image, which is controlled in the numerical study, is vulnerable to change as the iteration steps advance and may degrade when the amount of projection data is extremely limited (e.g. five views). In this work, we mask the image region that is unchanged from the prior image so that the masked region is not influenced by the updates during iterative steps. We show in numerical simulations that successful image reconstruction can be realized from five views. Images reconstructed by the TV algorithm with and without the prior image as the initial guess are also compared.

2 Methods

2.1 Formulation of the optimization problem

Image reconstruction for CT can be formulated as an inversion problem of a finite linear system, where the image and the measurement system are discretized. The imaging model is approximated by a discrete linear system as:

$$\vec{g} = M\,\vec{f}. \tag{1}$$

, where $\vec{f}$ is an $m-$vector representing the image function, $\vec{g}$ an $n-$vector corresponding to the projection data, and M represents the $m \times n$ system matrix. The constrained TV minimization algorithm is formulated as:

$$\begin{aligned} \vec{f}^{\star} &= \operatorname{argmin}||\vec{f}||_{\mathrm{TV}} \\ \text{subject to} \quad & |M\,\vec{f} - \vec{g}_{data}| \leq \epsilon, \quad \vec{f} \geq 0 \end{aligned} \tag{2}$$

, where $\vec{g}_{data}$ represents the measured data, and the inequality constraints correspond to the data fidelity at a given level of ϵ and positivity, respectively. $\vec{f}^{\star}$ is the solution of the inversion problem that minimizes image TV under the constraints. Image TV, in 2D for example, is given by

$$||\vec{f}||_{\mathrm{TV}} = \sum_{s,t} \sqrt{(f_{s,t} - f_{s-1,t})^2 + (f_{s,t} - f_{s,t-1})^2} \tag{3}$$

, where pixel values are labeled by $f_{s,t}$. The adaptive-steepest-descent projection-onto-convex-sets (ASD-POCS) method has been developed to implement this constrained optimization algorithm [5]. POCS algorithm finds images that respect the constraints of data fidelity and data positivity, and ASD algorithm searches for minimum-TV image.

2.2 Usage of prior image

When some part of the image is known from the prior image, the image reconstruction task can be considered a constrained optimization of the remaining part of the image only. Suppose $k\,(< m)$ components of $\vec{f}$ are known. We introduce a mask matrix D which is an $m \times m$ diagonal matrix such that $D_{ii} = 1$ if f_i is unknown and 0 otherwise. Note we used a single index for labeling $\vec{f}$ here. Mathematically, the data constraint in each iteration can be applied as

$$\vec{f} := \vec{f} + D\beta\vec{M}_i^{\mathrm{T}}\frac{g_i - \vec{M}_i \cdot \vec{f}}{\vec{M}_i \cdot \vec{M}_i}, \tag{4}$$

using the projection onto convex sets (POCS) method, where $\vec{M}_i^{\mathrm{T}}$ represents the transpose of the i^{th} row vector of M, and β the step size. Similarly, in the TV minimization step, it can be written as

$$\vec{f} := \vec{f} - D\gamma\hat{df}, \tag{5}$$

where $\hat{df}$ represents the normalized gradient descent of the image TV ($\hat{df} = \frac{\vec{df}}{|\vec{df}|}$, $\vec{df} = \nabla_{\vec{f}}||\vec{f}_{\mathrm{TV}}||$) and γ the step size. The initial guess of the image was set to be $\vec{f_0} = (I - D)\vec{f_P}$, where I represents the identity matrix and $\vec{f_P}$ the prior image. In other words, the initial image guess has the same image with the prior for the known region and zero for the unknown.

2.3 Numerical study

In order to show the feasibility of the proposed algorithm, we have conducted a numerical study for a 2-D circular, fan-beam geometry in this work. A simple phantom and a pelvis phantom (both in discrete form) as shown in Fig. 1 have been used to demonstrate high contrast and low contrast examples, respectively. Internal components have been shifted and/or deformed to prepare corresponding prior images. Difference images of the phantoms are shown in Fig.

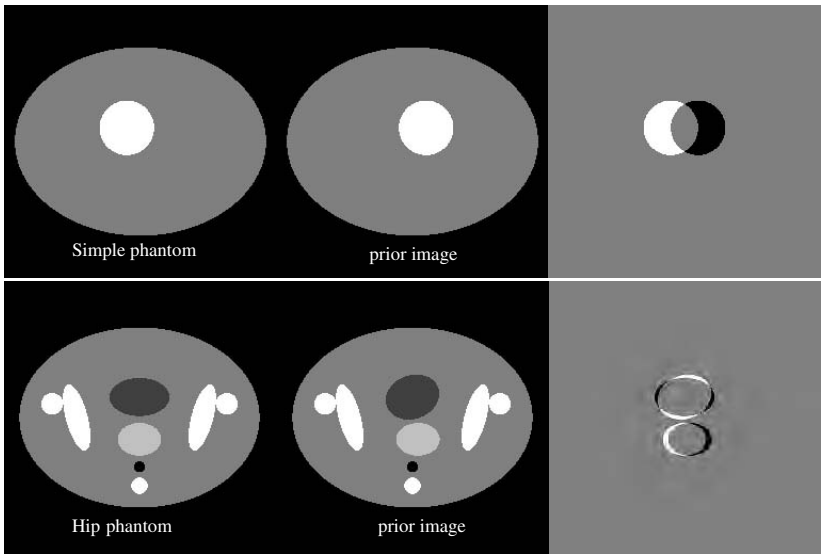

Figure 1: Simple phantom (top row) and pelvis phantom (bottom row). Prior images are shown in the middle column. Display window for the simple phantom is [0.99,1.01] and [0.96,1.04] for the pelvis phantom. Difference images are shown in the third column with the display window of [-0.01,0.01].

1 as well. Only five projections, as an extreme example of incomplete data, of the phantoms have been prepared in an equiangular fashion in this work. Image matrix size was 256×256, and the detector array size was 512.

For a given phantom the image reconstruction has been performed in three different manners: (case A) with no prior image, (case B) with the prior image as initial guess but without the use of mask matrix, and (case C) with the prior image as part of initial guess and with the use of mask matrix. For each case, the POCS-only algorithm, which is essentially an algebraic reconstruction technique, has also been applied for comparison. 500 iterations were completed for the simple phantom and 1000 iterations for the pelvis phantom; the maximum iteration numbers have been selected to guarantee images to convergence.

The mask matrix was prepared so that the diagonal components of it represent the weighting map. The weighting map should be carefully determined so that any changed pixels are included during the iterative updates. For the simple phantom the weighting map was prepared by use of the backprojection of the data difference between $\vec{g}_{data}$ (measured projection) and $\vec{g}_P$ (reprojection of the prior image). Appropriate thresholding after backprojection followed by smoothing have been applied to generate the weighting map. A binary map has been used in this work, where either 0 or 1 is assigned as a weighting value. The pentagon-like shape weighting map as shown in Fig. 2(c) was selected to be 1 and the remaining region to be zero. Therefore, only the region within the pentagon-like shape has been updated in each iteration step. The weighting map for the pelvis phantom has been prepared by manual definition based on the prior knowledge of the internal motion; a rectangular shape weighting map that includes changed components has been used. The boundaries of the weighting maps are shown on top of the phantom images in Fig. 3.

3 Results

The reconstructed images of the simple phantom are shown in Fig. 4. The first column of Fig. 4 corresponds to case A. The reconstructed images appear to be meaningless, which implies the algorithm without the prior image information

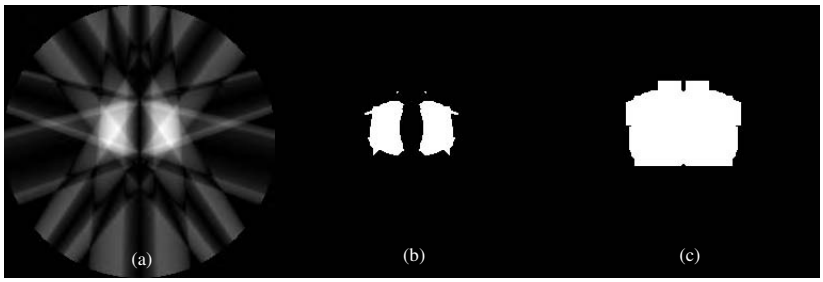

Figure 2: Process of generating a weighting map. (a) Absolute-valued image of backprojection of data difference. (b) Thresholded and digitized to a binary map. (c) Expanded map by use of smoothing and thresholding.

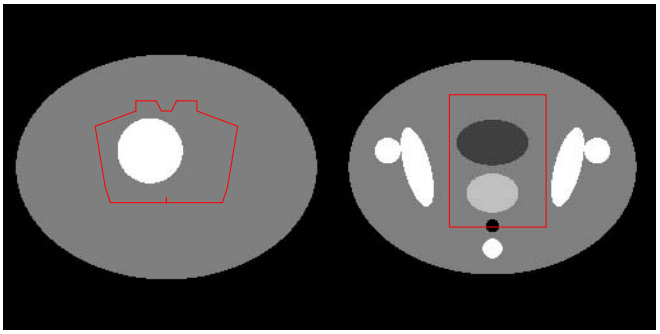

Figure 3: Weighting map boundaries are shown on top of the phantom images.

has ended up with a local minimum due to the extremely under-determinned situation. With the prior image as an initial guess (case B) as shown in the second column of Fig. 4, the images have been improved greatly compared to the results of case A. However, the images are far from the true image. In particular, the POCS-only image still contains a substantial prior image component. It is striking that the TV algorithm in case C successfully reconstructed the image as shown in the third column of Fig. 4, while the POCS-only still suffers.

The reconstructed images of the pelvis phantom are shown in Fig. 5. Similar behaviors of each case to the previous example can be found in Fig. 5. The prior image dominates the POCS-only reconstructed images in cases B & C, and the image reconstructed by the TV algorithm in case B has an overlap of the image components from the prior and the measurement. Only the TV algorithm in case C reconstructed the image successfully. Please note that the display window is wider than that used in the simple phantom case; the image error therefore shows up much more distinctly in the simple phantom case although the object is simpler.

4 Discussion and Conclusion

The prior image, which contains regions unchanged from the current image, reduces the under-determinedness of the linear imaging system. Depending on the amount of information that is translated from the prior image, the likelihood of ending in a local minimum that satisfy the data fidelity conditions decreases substantially.

The examples studied in this work are all idealized. With real data, inconsistency comes from a variety of sources: continuous nature of the object, imperfect scanning geometry calibration, physical data contamination such as scatter and beam hardening, and noise. Evaluation of the effects of those factors and correction methods for each of them are

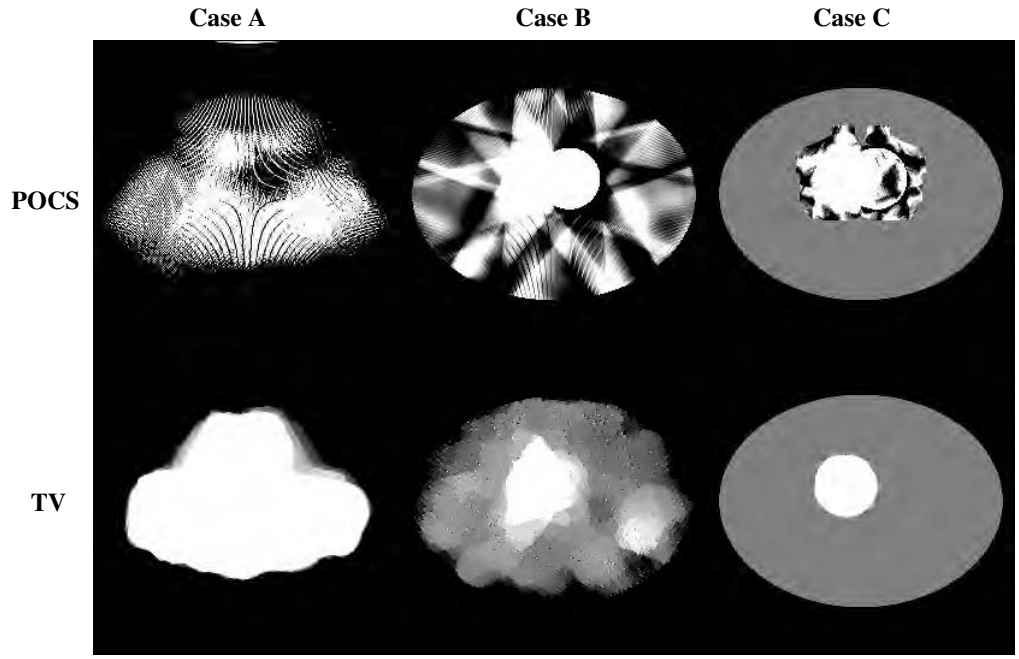

Figure 4: Reconstructed images of the simple phantom. No prior image information was used in case A (first-column) Case B (mid-column) represents the case using prior image as an initial guess but no weighting map, and case C (third-column) represents the case using both prior image and weighting map. Display window is [0.99,1.01].

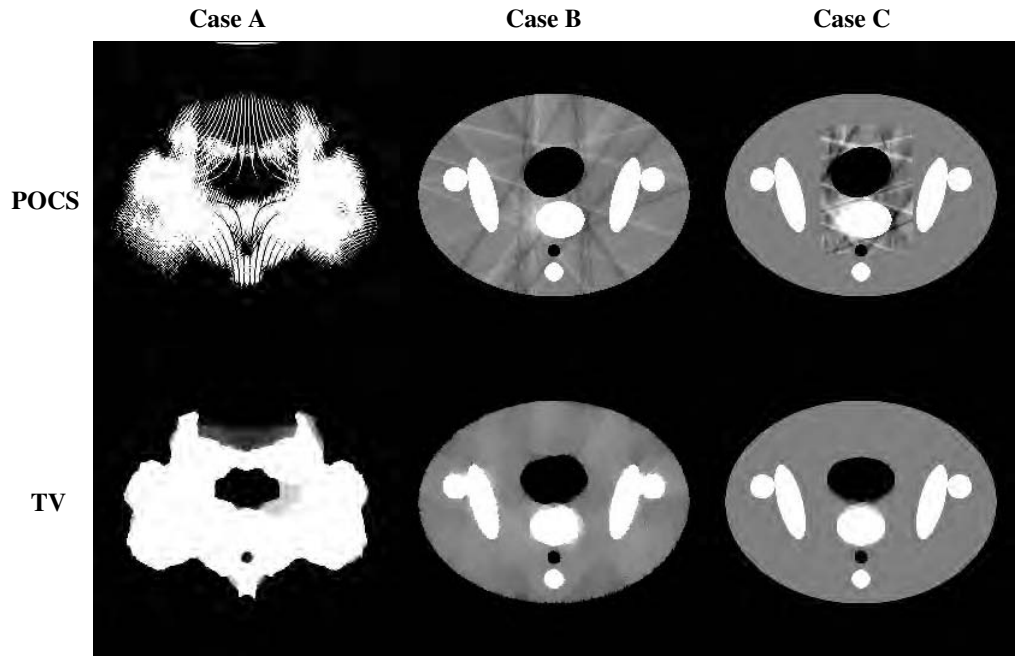

Figure 5: Reconstructed images of the pelvis phantom. Display window is [0.96,1.04].

under our investigation. Although we have demonstrated the performance of the proposed algorithm in a 2D fan-beam geometry, it is straightforward to extend the concept to 3D CBCT and numerical study results for 3D CBCT will be reported during the conference.

Practical applications of the proposed method to few-view CBCT-based IGRT may require an accurate image registration technique that correlates the few-view projections with the previous full-scan CBCT image. There exist many algorithms that can register the projections to the CBCT image quite accurately using bony structures. Defining a mask matrix (or a weighting map) can be a difficult task, but it can be done either by use of the backprojected data difference like the first example in this paper, by use of manual drawing or by expansion of the contoured organs based on empirical and statistical study. Please note that multiple disjoint regions can be locally updated using this technique.

In conclusion, we have successfully demonstrated that the TV algorithm with prior image and weighting map can reconstruct images from an extremely limited number of views from noiseless data in numerical studies.

5 Acknowledgments

S. Cho is supported in part by DOD predoctoral training grant PC061210. E. Pearson is supported by NIH predoctoral training grant T32 EB002103. This work was supported in part by National Institutes of Health grants R01EB00225, R01CA120540, and K01EB003913. Its contents are solely the responsibility of the authors and do not necessarily represent the official views of the National Institutes of Health.

References

[1] D. A. Jaffray, "Emergent technologies for 3-dimensional image-guided radiation delivery," *Semin. Radiat. Oncol.*, vol. 15, pp. 208–216, 2005.

[2] J. M. Balter and M. L. Kessler, "Imaging and alignment for image-guided radiation therapy," *J. Clin. Oncol.*, vol. 25, pp. 931–937, 2007.

[3] M. J. Murphy, J. Balter, S. Balter, J. A. Bencomo, I. J. Das, S. B. Jiang, C. M. Ma, G. H. Olivera, R. F. Rodebaugh, K. Ruchala, H. Shirato, and F. F. Yin, "The management of imaging dose during image-guided radiotherapy: Report of the AAPM Task Group 75," *Med. Phys.*, vol. 34, pp. 4041–4063, 2007.

[4] E. Y. Sidky, C. M. Kao, and X. Pan, "Accurate image reconstruction from few-views and limited-angle data in divergent-beam CT," *J. X-ray Sci. Tech.*, vol. 14, pp. 119–139, 2006.

[5] E. Y. Sidky and X. Pan, "Image reconstruction in circular cone-beam computed tomography by constrained, total-variation minimization," *Phys. Med. Biol.*, vol. 53, pp. 4777–4807, 2008.

[6] H. M. Shieh, C. L. Byrne, M. E. Testorf, and M. A. Fiddy, "Iterative image reconstruction using prior knowledge," *J. Opt. Soc. Am. A*, vol. 23, pp. 1292–1300, 2006.

[7] G. H. Chen, J. Tang, and S. Leng, "Prior image constrained compressed sensing (PICCS): A method to accurately reconstruct dynamic CT images from highly undersampled projection data sets," *Med. Phys.*, vol. 35, pp. 660–663, 2008.

[8] Y. Mameuda and H. Kudo, “New anatomical-prior-based image reconstruction method for PET/SPECT,” *IEEE NSS-MIC Conf. Rec.*, pp. M23–2, 2007.

[9] R. von Borries, C. J. Miosso, and C. Potes, “Compressed sensing using prior information,” *IEEE Comp. Adv. Multi. Sen. Adap. Proc.*, pp. 121–124, 2007.

[10] S. Cho, E. Y. Sidky, J. Bian, C. A. Pelizzari, and X. Pan, “A preliminary investigation of using prior information for potentially improving image reconstruction in few-view CT,” in *Medical Imaging*, vol. 6913 of *Proc. SPIE*, p. 69132C, 2008.